Key Processes Associated with the Diurnal Cycle of Rainfall over East Amazon and Their Representation in Global Climate Models

XIANAN JIANG,[a,b] PATRICK CALLAGHAN,[c] ADAM HERRINGTON,[c] JULIO BACMEISTER,[c] RONG FU,[a,d] JOAO TEIXEIRA,[a,b] AND RICHARD B. NEALE[c]

[a] *Joint Institute for Regional Earth System Science and Engineering, University of California, Los Angeles, Los Angeles, California*
[b] *Jet Propulsion Laboratory, California Institute of Technology, Pasadena, California*
[c] *National Center for Atmospheric Research, Boulder, Colorado*
[d] *Department of Atmospheric and Oceanic Sciences, University of California, Los Angeles, Los Angeles, California*

(Manuscript received 26 February 2025, in final form 17 April 2026, accepted 22 July 2026)

ABSTRACT: Precipitation in the Amazon basin is vital for the global hydrological and carbon cycles. However, current global climate models, which typically operate at horizontal resolutions of approximately 100 km, exhibit significant shortcomings in accurately representing precipitation patterns in the Amazon. Notably, these models suffer from a persistent dry bias over east Amazon during the local rainy season from March to May. This deficiency largely stems from the models' inability to accurately capture the formation and southwestward inland propagation of diurnal rain belts that initiate along the northeast coast of Brazil. Observational diagnoses show that these diurnal rain events are closely linked to the westward propagation of lower-tropospheric buoyancy fluctuations resulting from moisture advection by the easterly Amazon low-level jet. Model experiments utilizing regionally refined grids indicate that the representation of these diurnal rain belts, and consequently the mean precipitation pattern in east Amazon, is significantly improved in higher-resolution model simulations (from 25 to 6 km). Further analysis reveals that this improved diurnal cycle of precipitation is primarily due to a substantial increase in resolved large-scale precipitation that responds to lower-tropospheric buoyancy forcing as the model resolution increases.

KEYWORDS: Amazon region; Cloud resolving models; Diurnal effects

1. Introduction

The Amazon rainforest, the largest tropical forest on Earth, plays a pivotal role in maintaining Earth's energy, moisture, and carbon balances. It accounts for approximately 20% of the world's freshwater discharge and around 15% of global terrestrial photosynthesis (Field et al. 1998; Foley et al. 2002; Phillips et al. 2017). Changes in Amazonian precipitation not only impact the regional water and energy balance but also influence global carbon–climate feedbacks and atmospheric CO_2 concentrations (Cox et al. 2004). Precipitation variations in the Amazon region also exert far-reaching impacts on global atmospheric circulation and climate variability. Specifically, latent heat release from convection in the Amazon plays an active role in modulating the easterly equatorial trade winds and the intertropical convergence zone (ITCZ) over the Atlantic Ocean (Biasutti et al. 2005; Wang and Fu 2007; Richter et al. 2014; Bai and Schumacher 2021). In turn, these trade winds significantly shape the zonal and meridional sea surface temperature gradients, driving major climate variability modes over the Atlantic Ocean, including the Atlantic Niño and the Atlantic meridional mode, and even influencing the North Atlantic Oscillation in mid- to high latitudes (Xie and Carton 2004; Xie 2023).

However, state-of-the-art climate models demonstrate significant biases in their representation of historical rainfall climatology and considerable intermodel spread in projecting future rainfall changes across the Amazon basin (e.g., Fu et al. 2013; Li et al. 2006; Vera et al. 2006; Yin et al. 2013; Richter et al. 2014; Zhang et al. 2017). Persistent dry biases in the Amazon have been reported in recent generations of climate models participating in the Coupled Model Intercomparison Project (CMIP; Meehl et al. 2005), including the latest CMIP phase 6 (CMIP6) (Richter and Xie 2008; Richter et al. 2014; Richter and Tokinaga 2020; Tian and Dong 2020; Hagos et al. 2021). This precipitation deficit is closely associated with westerly wind biases over the equatorial Atlantic and the associated southward shift of the Atlantic ITCZ, often manifesting as the persistent "double ITCZ" bias in model simulations (Tozuka et al. 2011; Richter et al. 2014; Tian and Dong 2020; Bai and Schumacher 2021; Jiang and Tian 2024). The inability of these models to accurately represent Amazonian rainfall fundamentally limits our predictive skill for both regional weather extremes and global climate patterns and is considered a major source of uncertainty in projecting future atmospheric CO_2 concentrations and resulting climate changes (e.g., Friedlingstein et al. 2006, 2014).

This study was largely motivated by persistent dry biases in the mean precipitation pattern in the Amazon, particularly over the east Amazon region off the northeastern Brazilian coast, in a developmental version of the next generation Community Atmosphere Model (CAM; hereafter CAM6+), following the

Supplemental information related to this paper is available at the Journals Online website: https://doi.org/10.1175/JCLI-D-25-0110.s1.

Corresponding authors: Xianan Jiang, xianan@ucla.edu; Patrick Callaghan, patc@ucar.edu.

DOI: 10.1175/JCLI-D-25-0110.1

earlier generations of CAM models (Gent et al. 2011; Danabasoglu et al. 2020; Bai and Schumacher 2021). With a maximum annual precipitation occurring during boreal spring from March to May (MAM), precipitation in east Amazon is well known for its distinct diurnal cycle, often manifested as organized mesoscale convective systems (MCSs; Feng et al. 2021; Tai et al. 2021; Anselmo et al. 2021). A prominent form of these diurnal precipitation systems is the development of squall lines that orient parallel to the Northeast Brazilian coast and systematically propagate inland (Cohen et al. 1995; Silva Dias and Ferreira 1992; Garreaud and Wallace 1997; Burleyson et al. 2016; Oliveira and Oyama 2020; Sousa et al. 2021). These propagating systems are typically initiated by local land–sea breezes in the coastal areas (Kousky 1980; Sousa et al. 2021).

While model biases in representing the mean precipitation pattern over the Amazon can often be attributed to deficiencies in subgrid physical parameterizations (e.g., Xie et al. 2019; Tai et al. 2021), they may also arise from the relatively coarse horizontal resolution of current climate models, which is typically about 100 km, including CAM6+. Recent advancements in supercomputing technology have enabled the integration of climate models at a horizontal resolution of several kilometers over the global domain (Satoh et al. 2019; Stevens et al. 2019; Herrington and Reed 2020; Caldwell et al. 2021; Lin et al. 2023) or over specific regions using the so-called regionally refined modeling technique (e.g., Bambach et al. 2022; Sakaguchi et al. 2023). These global or regionally refined convection-permitting models demonstrate significant improvements over the coarse resolutions of traditional global climate models (GCMs), particularly in their representation of precipitation and convection (Miura et al. 2007; Caldwell et al. 2021).

In this study, by leveraging a series of simulations from the newly developed regionally refined high-resolution CAM6 with various horizontal resolutions over South America (hereafter, RR-CAM6), along with high-resolution rainfall observations and reanalysis datasets, we address the following questions: How are model biases in representing the diurnal cycle of precipitation related to their biases in simulating mean precipitation over east Amazon? What are the key processes underlying the observed diurnal evolution of precipitation in this region? Can the representation of the diurnal cycle of precipitation and the mean precipitation pattern over east Amazon be improved in high-resolution RR-CAM6 simulations? If so, what key physical processes contribute to this improvement? Addressing these questions will not only advance our understanding of rainfall processes over east Amazon but also offer valuable guidance for model development, ultimately leading to improved simulations of precipitation variability over South America.

The remainder of this paper is organized as follows. Section 2 describes the observational datasets and the CAM6+ model, as well as the high-resolution RR-CAM6 experiments analyzed in this study. Section 3 illustrates model biases in simulating the seasonal mean precipitation pattern over east Amazon during MAM in CMIP6 models and CAM6+. We then present the role of the diurnal cycle in determining the MAM mean precipitation over east Amazon, the key processes regulating the propagation of diurnal precipitation based on observations, and biases in representing the diurnal cycle of precipitation over east Amazon in CAM6+. Additionally, this section examines the representation of the diurnal cycle of precipitation in the RR-CAM6 experiments at various horizontal resolutions and explores the processes that contribute to the improvement in diurnal rainfall propagation in high-resolution RR-CAM6 simulations. Finally, section 4 presents a summary and discussion of the main findings.

2. Observational and model datasets

a. *Observational datasets*

The rainfall observations from the Global Precipitation Measurement (GPM) mission, specifically the Integrated Multi-satellitE Retrievals for GPM (IMERG, version 7), are used to characterize diurnal precipitation evolution over east Amazon. The GPM IMERG algorithm unifies precipitation observations from the GPM Microwave Imager and the Dual-Frequency Precipitation Radar on the GPM Core Observatory, along with sensors from a constellation of other satellites, including passive microwave and infrared sensors, calibrated by gauge data. IMERG provides a global precipitation product with high-resolution, half-hourly precipitation estimates gridded at a spatial resolution of 0.1° since 2000 (Huffman et al. 2019). For this study, hourly averaged IMERG rainfall observations from 2010 to 2019 are employed.

The fifth generation European Centre for Medium-Range Weather Forecasts (ECMWF) atmospheric reanalysis (ERA5; Hersbach et al. 2020) is analyzed to identify key processes associated with the diurnal evolution of precipitation over east Amazon. ERA5 was generated using 4D-Var data assimilation in the ECMWF's Integrated Forecasting System (IFS). It features a horizontal resolution of approximately 30 km at hourly time intervals, with a total of 137 hybrid sigma/pressure model levels in the vertical, extending up to a top level of 0.01 hPa. Variables analyzed in this study include 3-hourly vertically interpolated 3D variables (winds, moisture, and temperature) at 27 pressure levels between 1000 and 100 hPa for the period from 2010 to 2019.

In addition to the ERA5 reanalysis, detailed moisture budget terms generated by the ECMWF-IFS for the Year of Polar Prediction (YOPP) Project (Bauer et al. 2020) were also analyzed to identify the key processes regulating moisture variability associated with the diurnal evolution of precipitation over east Amazon. The EC-YOPP dataset includes initial condition and forecast model outputs from the ECMWF-IFS with 3-hourly tendency terms for various physical and dynamical processes. It has a horizontal resolution of about 18 km at 91 vertical levels for the period from 1 May 2017 to 31 October 2019. In this study, we analyzed the EC-YOPP dataset for the MAM season of 2018–19 to examine the moisture budget processes associated with the diurnal propagation of precipitation over east Amazon.

b. *The CAM6+ GCM*

The CAM6+ GCM analyzed in this study is an updated version of CAM6 that was used for the National Center for

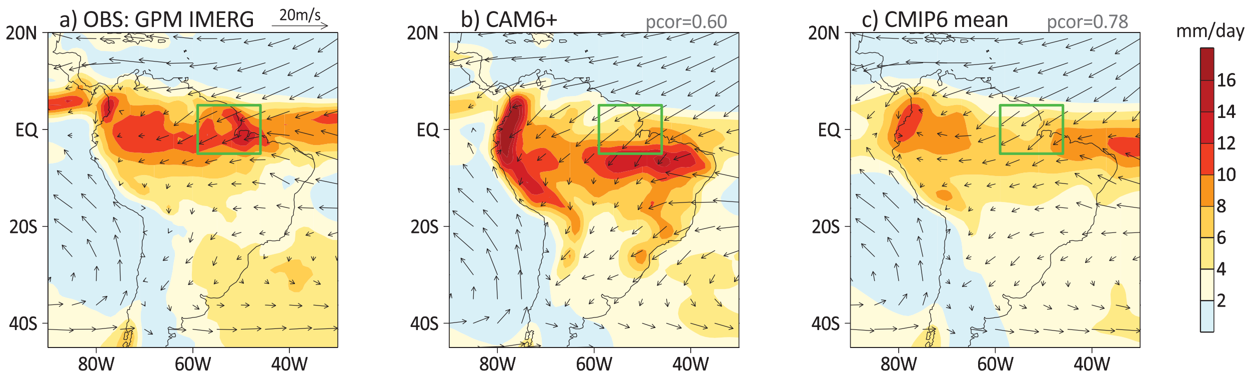

FIG. 1. Mean precipitation (shaded with the color bar; mm day^{-1}) and wind at 900 hPa [see the scale on the upper right of (a)] during MAM over South America based on (a) observations (IMERG; 2010–19), (b) CAM6+ (1998–2007), and (c) CMIP6 model ensembles (1980–2014). The green box (60°–45°W; 5°S–5°N) in each plot denotes the northeastern coastal region of Brazil, the focus of this study, and referred to as east Amazon in the text. All fields in the three panels are interpolated onto 1° grids. Pattern correlation coefficients between simulated and observed mean precipitation patterns are shown on the upper right of each panel. CMIP6 simulations are based on coupled historical simulations (see Fig. S2 for models included).

Atmospheric Research (NCAR)'s participation in the CMIP6 project (Danabasoglu et al. 2020). The main updates include a new spectral-element (SE) dynamical core and enhanced vertical resolution from 32 to 58 vertical levels, while largely retaining the physical schemes of CAM6, including the Cloud Layers Unified by Binormals (CLUBB) unified turbulence scheme for shallow-convection and the boundary layer (Golaz et al. 2002; Larson 2017), the Rapid Radiative Transfer Model for GCMs (RRTMG) radiation package (Iacono et al. 2008), the Modular Aerosol Model (Liu et al. 2016), the second version of the Morrison–Gettelman cloud microphysics scheme (Gettelman and Morrison 2015), and the Zhang–McFarlane deep convection scheme (Zhang and Mcfarlane 1995).

Atmospheric Model Intercomparison Project (AMIP)-type experiments based on the CAM6+ were conducted for 10 years from 1998 to 2007 with prescribed monthly sea surface temperature and sea ice datasets over the ocean (Hurrell et al. 2008) while coupling with the dynamic Community Land Model, version 5 (Lawrence et al. 2019), over land. A horizontal resolution of about 100 km with 58 vertical levels is applied for the CAM6+ experiments.

c. Regionally refined CAM6 (RR-CAM6) model experiments

The diurnal cycle of precipitation over east Amazon was also analyzed using simulations from a series of standard CAM6 experiments that utilize regionally refined grids over South America, with horizontal resolutions ranging from approximately 100 km in the "ne30" experiment, 50 km in the "ne60" experiment, 25 km in the "ne120" experiment, 12 km in the "ne240" experiment, and 6 km in the "ne480" experiment. For regions beyond the regionally refined grids over South America, a uniform horizontal resolution of about 100 km is maintained across all experiments, with 3D model fields, including temperature, specific humidity, and winds, strongly nudged toward the hourly ERA5 reanalysis data with a relaxation time of 1 h. (See Fig. S1 in the online supplemental material for an example of the model grid configuration for the ne240 experiment.) Note that the Zhang–McFarlane convection scheme remains active to represent subgrid cumulus processes in all these RR-CAM6 experiments. Due to limited computational resources, all of these RR-CAM6 experiments are integrated for 3 years, including June 2010–May 2011, June 2015–May 2016, and June 2018–May 2019, representing conditions associated with the La Niña, El Niño, and neutral El Niño–Southern Oscillation phases, respectively.

In the following discussion, we will focus primarily on the rainy season over east Amazon from March to May. During this period, the diurnal cycle of local precipitation is particularly pronounced, and climate models struggle to accurately simulate the local mean patterns of precipitation and their variability, as will be illustrated below. Hereafter, unless stated otherwise, we will specifically refer to east Amazon as the coastal area of northeastern Brazil (60°–45°W; 5°S–5°N), shown by the green box region in Fig. 1, for the sake of brevity. Note that despite the different time periods analyzed across these datasets, the climatological mean precipitation and diurnal cycle shown in this study are robust and not sensitive to minor variations in the selected periods, as will be demonstrated later using the GPM-IMERG dataset.

3. Results

a. Seasonal mean precipitation over east Amazon in CAM6+ and CMIP6 models

Figure 1 illustrates the observed and simulated MAM seasonal mean precipitation and wind patterns over the South American sector. The observed rainfall pattern over the Amazon during MAM is largely characterized by a zonally elongated rain belt near the equator, which is connected to the ITCZ over the Atlantic to the east. A local precipitation maximum is observed in the northeastern coastal region of Brazil (highlighted in the green box in Fig. 1a). However, pronounced precipitation deficits in the MAM mean rainfall pattern over east Amazon are found in CAM6+, resulting from

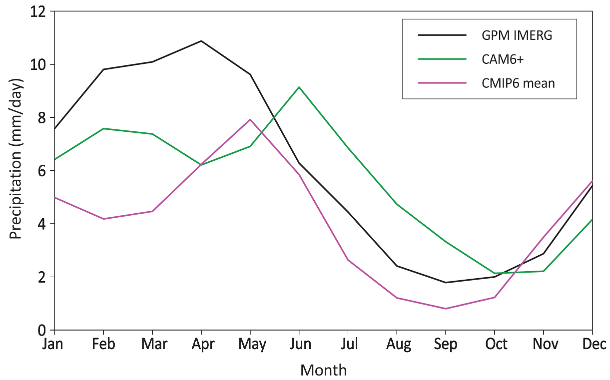

FIG. 2. Annual cycle of climatological mean precipitation over east Amazon (the green box in Fig. 1) based on IMERG observations (black), CAM6+ (green), and the CMIP6 model ensemble mean (pink). CMIP6 simulations are based on coupled historical simulations during 1980–2014 (see Fig. S2 for models included).

a southward shift of the rainfall belt from the equator (Fig. 1b). This southward-shifted rain belt over east Amazon in CAM6+ is closely associated with a southward shift of the low-level convergence zone. Additionally, CAM6+ also exhibits notable biases over the Andes, with significantly overestimated precipitation along the mountain range compared to IMERG, although satellite-measured precipitation could also be underestimated over high-elevation regions (e.g., Lober et al. 2023). A relatively low pattern correlation score of 0.6 for mean MAM precipitation in South America is found in CAM6+ when compared to IMERG. Meanwhile, the multimodel ensemble MAM mean precipitation pattern simulated in CMIP6 models exhibits two disconnected precipitation maxima over equatorial South America: one along the Pacific coast and the other over the Atlantic ITCZ region, leading to dry biases in the eastern part of the Amazon region (Fig. 1c). As previously discussed, this significant underestimation of mean MAM precipitation over east Amazon is a common model bias, as shown across the individual CMIP6 model simulations (see Fig. S2).

Model deficiencies in simulating mean precipitation during MAM over the east Amazon region are further illustrated by the climatological annual cycle of precipitation, averaged over the green box shown in Fig. 1 for both IMERG and simulations (Fig. 2). In contrast to a pronounced peak in precipitation during MAM in observations, the simulated mean precipitation in this period is significantly weaker in both CAM6+ and the CMIP6 GCMs, resulting in a biased and weakened annual cycle of local precipitation in model simulations. While the most substantial model deficiencies in east Amazon precipitation for CAM6+ are found in MAM, significant precipitation deficits are also found in February in the coupled CMIP6 models, which can be partially associated with model deficiencies in SST patterns in these coupled models (e.g., Richter and Tokinaga 2020). In the following section, we mainly focus our analyses on the east Amazon region during MAM, aiming to understand the key processes responsible for the significant dry biases in CAM6+ with the aid of RR-CAM6 simulations.

b. *Representation of the diurnal cycle of precipitation over east Amazon in CAM6+*

The precipitation during the rainy season over east Amazon exhibits a pronounced diurnal cycle (Tai et al. 2021; Zhuang et al. 2017; Burleyson et al. 2016; Anselmo et al. 2021; Feng et al. 2021). Figure 3 illustrates the climatological diurnal cycle of precipitation during MAM in CAM6+ simulations, along with observations from IMERG. Since the daily integrated precipitation over a climatological diurnal cycle on each grid point corresponds to its seasonal mean precipitation, examining the climatological diurnal cycle of precipitation in CAM6+ simulations is crucial for understanding the significant model biases in seasonal mean precipitation over east Amazon.

As shown in Fig. 3a, the observed precipitation over east Amazon is characterized by the southwestward movement of an elongated rain belt that runs parallel to the northeastern Brazil coastline. This pattern resembles the squall lines associated with the diurnal cycle of precipitation in this region, as previously reported (Cohen et al. 1995; Silva Dias and Ferreira 1992; Oliveira and Oyama 2020). The coastal rain belt typically forms near local noon and develops significantly along the coastline at 1400 LT. After reaching peak intensity around 1700 LT, the rain belt migrates southwestward inland during the late afternoon and nighttime, albeit with reduced intensity. By 1100 LT the following day, the propagating rain belt arrives at the equatorial central Amazon near 60°W, where it tends to intensify rapidly after 1400 LT, possibly due to substantial convective available potential energy resulting from local surface warming. Recent observational studies suggest that heavy precipitation along the coastal diurnal rain belt is dominated by MCS activity over the southern part of east Amazon, while MCSs only play a minor role over the northern part (Anselmo et al. 2021; Feng et al. 2021). It is important to note that while the composite illustrates a smooth, continuous propagation of the diurnal rain belt from the coast inland to approximately 60°W, individual diurnal convective systems may not complete this full migration during a single life cycle.

In the CAM6+ simulations (Fig. 3b), while the coastal rain belt over east Amazon is discerned in the afternoon between 1400 and 1700 LT, its intensity is noticeably weaker compared to IMERG, and the location of the rainfall maxima shifts slightly away from the green box region seen in the observations, in agreement with the significant dry bias identified in the mean MAM precipitation pattern in this model (Fig. 1).

The deficiencies in CAM6+ in accurately depicting the diurnal southwestward-propagating rain belt over east Amazon are clearly shown in Hovmöller diagrams of diurnal precipitation in Fig. 4. These Hovmöller diagrams are plotted along a transect roughly following the propagation direction of the rain belt in observations (denoted by the blue line AB in Fig. 3, 1400 LT, left column), with precipitation averaged over a 10° belt centered along the blue line. The vertical dashed lines in Fig. 4 denote the approximate location of the coastline over northeastern Brazil along the transect. While observations indicate that convection triggers near the coast at noon and systematically migrates southwestward inland (Fig. 4a), these

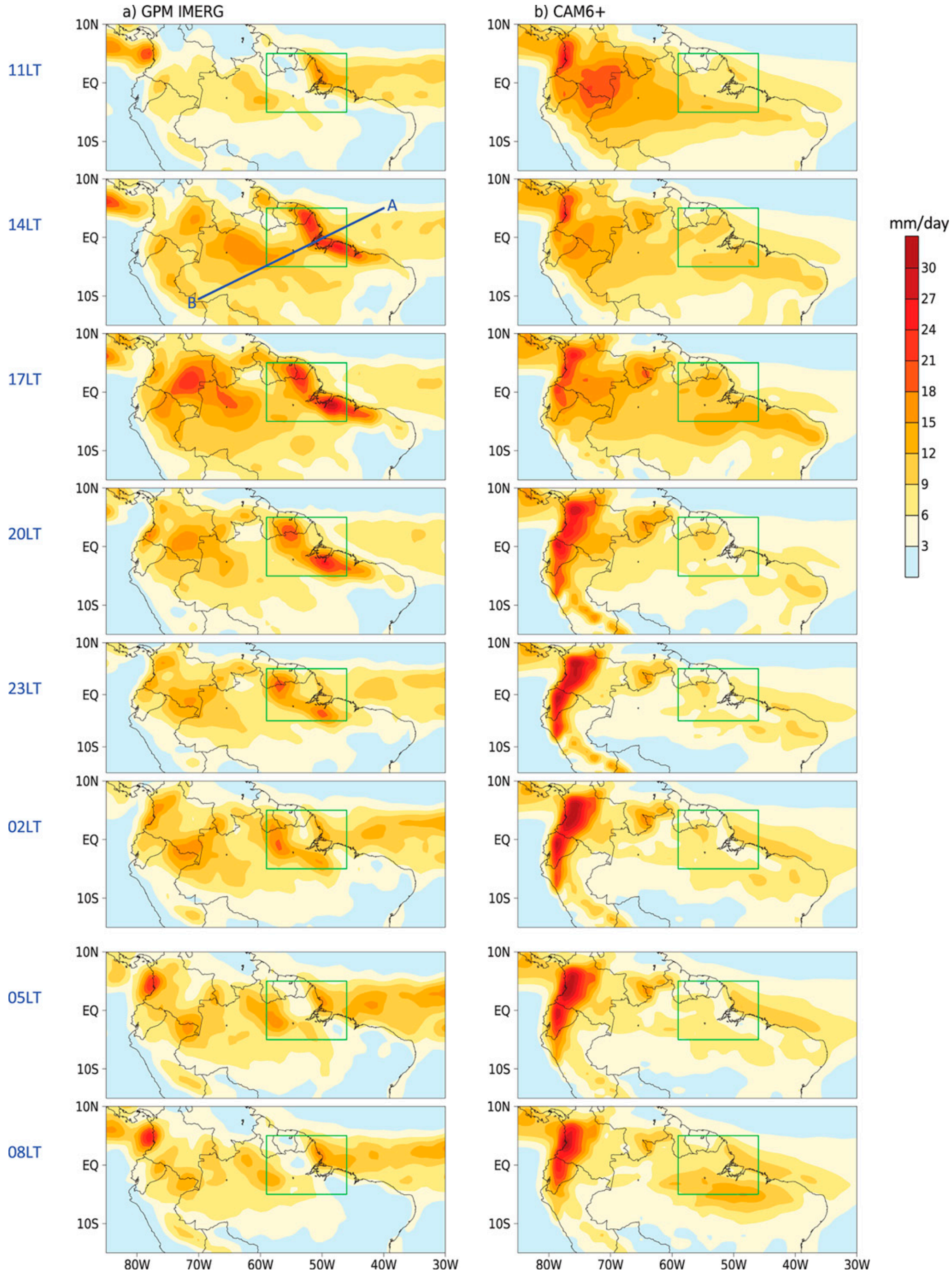

FIG. 3. The climatological diurnal evolution (3 hourly) of precipitation over tropical South America during MAM based on (a) IMERG and (b) CAM6+. Local time is defined at the longitude of 60°W. The transect shown by the blue line (AB) on the left panel at 14 LT roughly denotes the observed southwestward propagation direction of coastal rain belts.

propagating convection signals are largely absent in CAM6+ simulations. The results in Figs. 3 and 4 suggest that the significant dry biases in MAM mean precipitation over east Amazon in CAM6+, and possibly other CMIP6 models, are closely related to their inability to accurately represent the regional diurnal cycle of precipitation. This result will be further illustrated with additional observational evidence in the following sections.

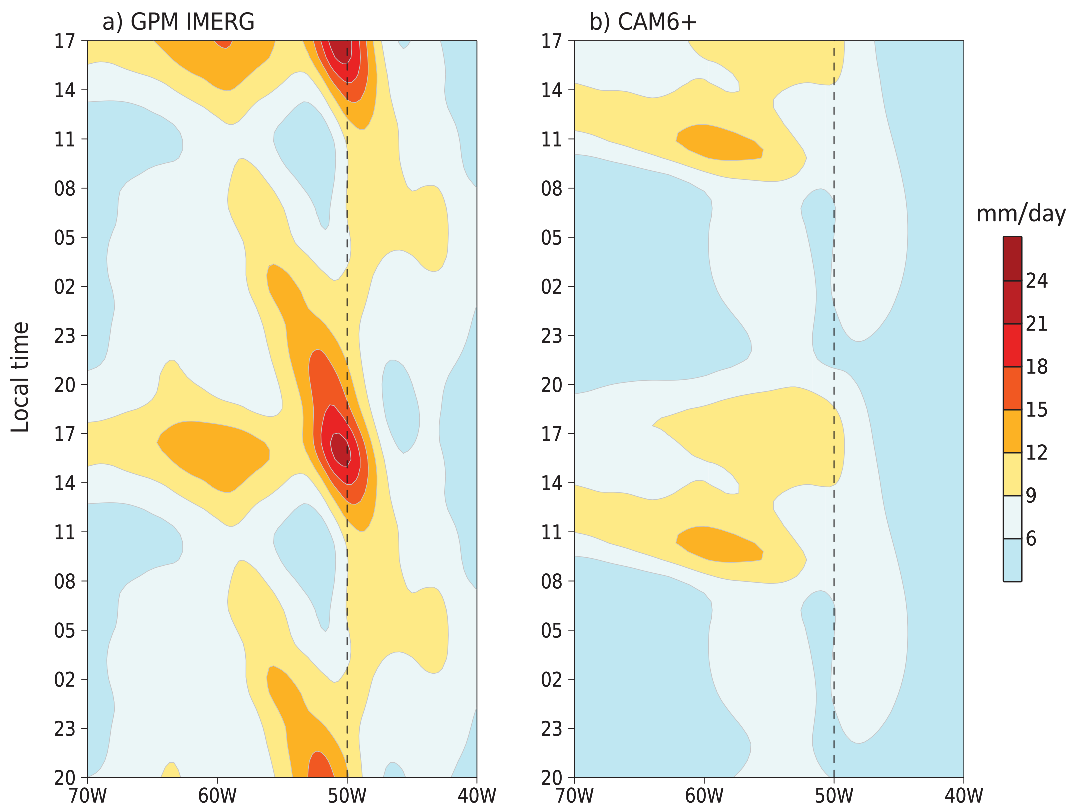

FIG. 4. Hovmöller diagram of precipitation along the transect following the southwestward propagating diurnal rain belt (averaged over a 10° belt centered along the blue line AB in Fig. 3) based on the climatological diurnal cycle during MAM for (a) IMERG and (b) CAM6+. Note that the time span on the *y* axis in each panel is repeated for 2 days. The dashed lines indicate the approximate location of the coastline over equatorial South America along the transect.

c. *Key processes driving the westward-propagating diurnal rain belt over east Amazon*

Considering the significant model deficiency in capturing the observed westward-propagating diurnal rain belts over east Amazon in CAM6+, and its close association with model bias in the seasonal mean precipitation pattern, this section focuses on observations to identify key processes regulating the westward propagation of diurnal precipitation over east Amazon.

In the following discussion, we consider the diurnal cycle of precipitation over east Amazon on each day as a diurnal event. Following a previous study on the diurnal cycle of precipitation in the Great Plains (Jiang et al. 2006), we employ an extended empirical orthogonal function (EEOF) analysis to identify days with strong and weak propagating precipitation signals over east Amazon. The EEOF analysis is conducted using 3-hourly IMERG precipitation data over eastern Amazon (60°–40°W, 6°S–4°N; as shown in Fig. 5) for the period from 2010 to 2019, with a total of seven time lags. Before conducting the EEOF analysis, the long-term climatological annual cycle (annual mean plus three leading annual harmonics) was removed from the precipitation data. The derived eigenvectors from the EEOF analysis represent a series of evolution patterns associated with the leading modes. The first and second modes ($EEOF_1$ and $EEOF_2$) capture the same leading mode of diurnal precipitation variability over east Amazon (Fig. 5), characterized by a largely southwestward propagation from the coastal region toward the inland areas, consistent with the observed composite climatological diurnal evolution patterns shown in Fig. 3, but with a 90° phase difference between the $EEOF_1$ and $EEOF_2$.

To derive the daily amplitude of the leading diurnal propagating mode over east Amazon from 2010 to 2019, we calculate the daily mean of 3-hourly combined amplitude based on the two principal components (PCs), i.e., $\sqrt{PC_1^2 + PC_2^2}$. Strong diurnal propagation events can then be identified for days with their daily amplitude of the leading diurnal EEOF mode exceeding the long-term mean amplitude plus one standard deviation, while weak events are identified as those with daily amplitude below the long-term mean amplitude minus one standard deviation.

During the MAM period from 2010 to 2019, we identified a total of 162 strong propagating diurnal events and 158 weak diurnal events. By the design of this approach, pronounced westward propagation of diurnal precipitation over east Amazon is evident in the Hovmöller diagram along the transect AB based

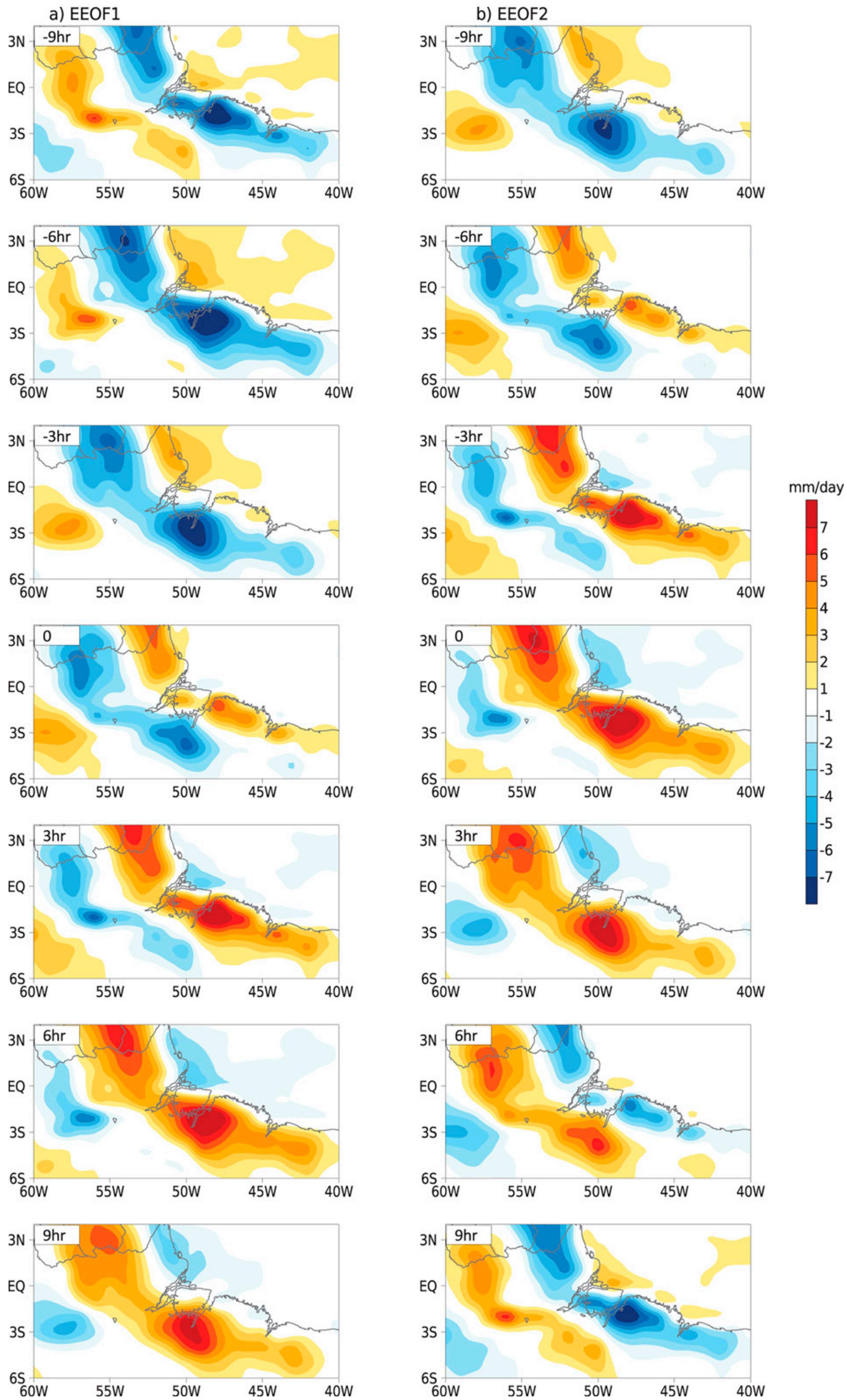

FIG. 5. Evolution patterns of diurnal precipitation anomalies of the first two leading eigenvectors derived by the EEOF analysis of 3-hourly IMERG precipitation over east Amazon for the period of 2010–19.

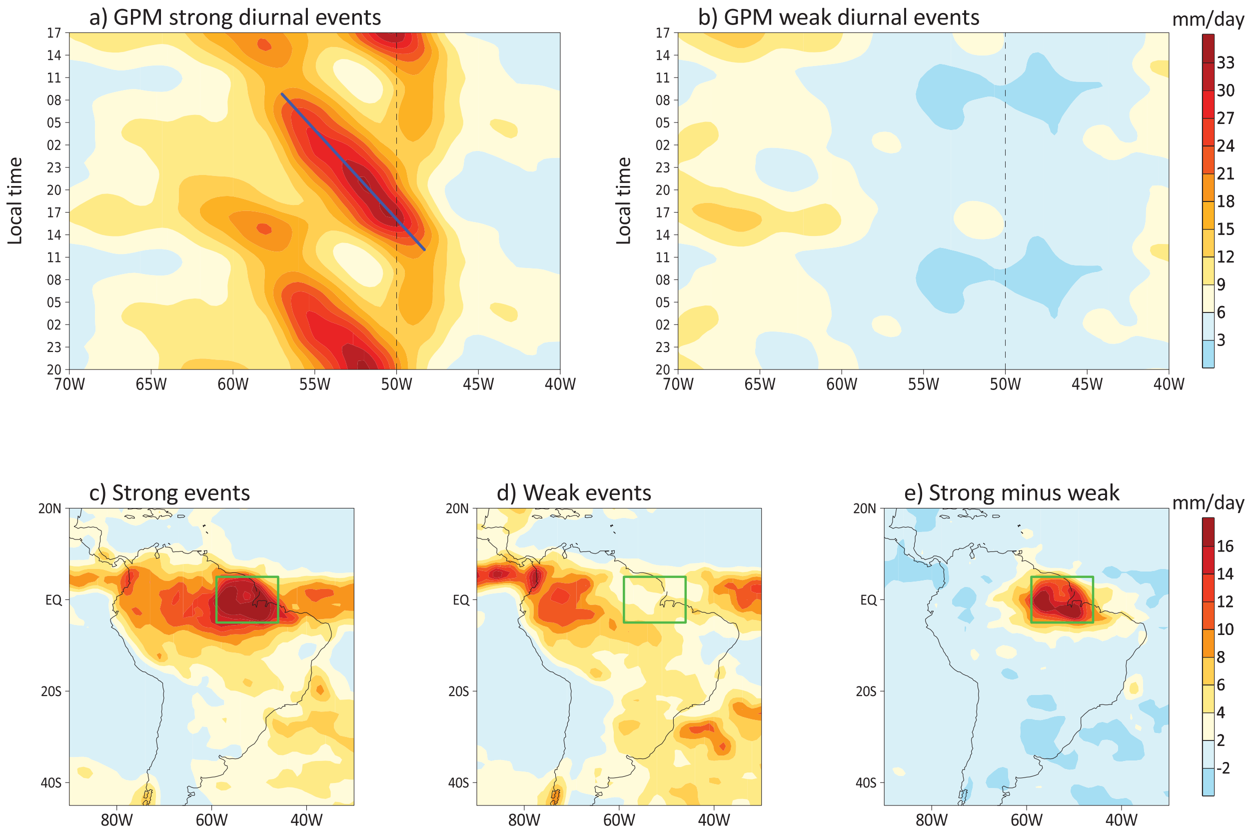

FIG. 6. (top) As in Fig. 4, but for Hovmöller diagrams of diurnal precipitation associated with (a) strong and (b) weak diurnal propagation events. As in Fig. 4, these Hovmöller diagrams are derived by averaged precipitation over a 10° belt along the transect following the blue line AB in Fig. 3. (bottom) Daily mean precipitation patterns based on (c) strong and (d) weak diurnal propagation events, and (e) their differences. All these results are based on IMERG observations with units of millimeters per day.

on composites of strong events (Fig. 6a). In contrast, westward-propagating diurnal precipitation signals are largely absent in the composite of weak diurnal events (Fig. 6b). Notably, for the strong diurnal propagation events, strong convection tends to establish near the coastal region around noon, with the maximum amplitude occurring during the afternoon and early evening. The systematic westward migration of these strong diurnal events can extend to 60°W by the following morning, with a propagation speed of approximately 14 m s^{-1} (Fig. 6a), which is highly consistent with the phase speeds of Amazon coastal MCSs or squall lines previously reported (Cohen et al. 1995; Sousa et al. 2021; Anselmo et al. 2021). Figures 6c and 6d further illustrate the mean precipitation patterns for composites of strong and weak diurnal propagation events, respectively. A significant influence of westward-propagating diurnal events on the mean precipitation over east Amazon is readily seen in Fig. 6c. In contrast, much weaker mean precipitation is observed during days when the westward-propagating diurnal precipitation events are inactive (Fig. 6d). The differences in the mean precipitation between strong and weak diurnal events as shown in Fig. 6e further suggest that the activity of diurnal propagation modes significantly contributes to the mean precipitation over east Amazon. This observational evidence confirms that the diurnally forced westward-propagating convective systems from the northeastern Brazil coast are an essential mode of precipitation variability over east Amazon. However, these diurnal propagating precipitation events are largely underestimated in CAM6+ (Figs. 3 and 4), resulting in a significant model dry bias over east Amazon. The results in Fig. 6 also indicate that the prevailing diurnal precipitation mode over east Amazon does not significantly affect precipitation over the western Amazon; therefore, different mechanisms may be responsible for the dry biases over the west and east of the Amazon (e.g., Cui et al. 2021).

To gain insights into the processes responsible for the model deficiencies in representing the diurnal propagating mode over east Amazon, a critical question needs to be addressed: What are the key processes that drive the observed westward propagation of diurnal convection over east Amazon? Motivated by a recently proposed precipitation-buoyancy framework that highlights a close relationship between the lower-tropospheric buoyancy B_L and tropical convection (Ahmed and Neelin 2018; Ahmed et al. 2020; Ahmed and Neelin 2021; Adames et al. 2021), we investigate how diurnal changes in B_L can potentially contribute to the westward propagation of convection over east Amazon.

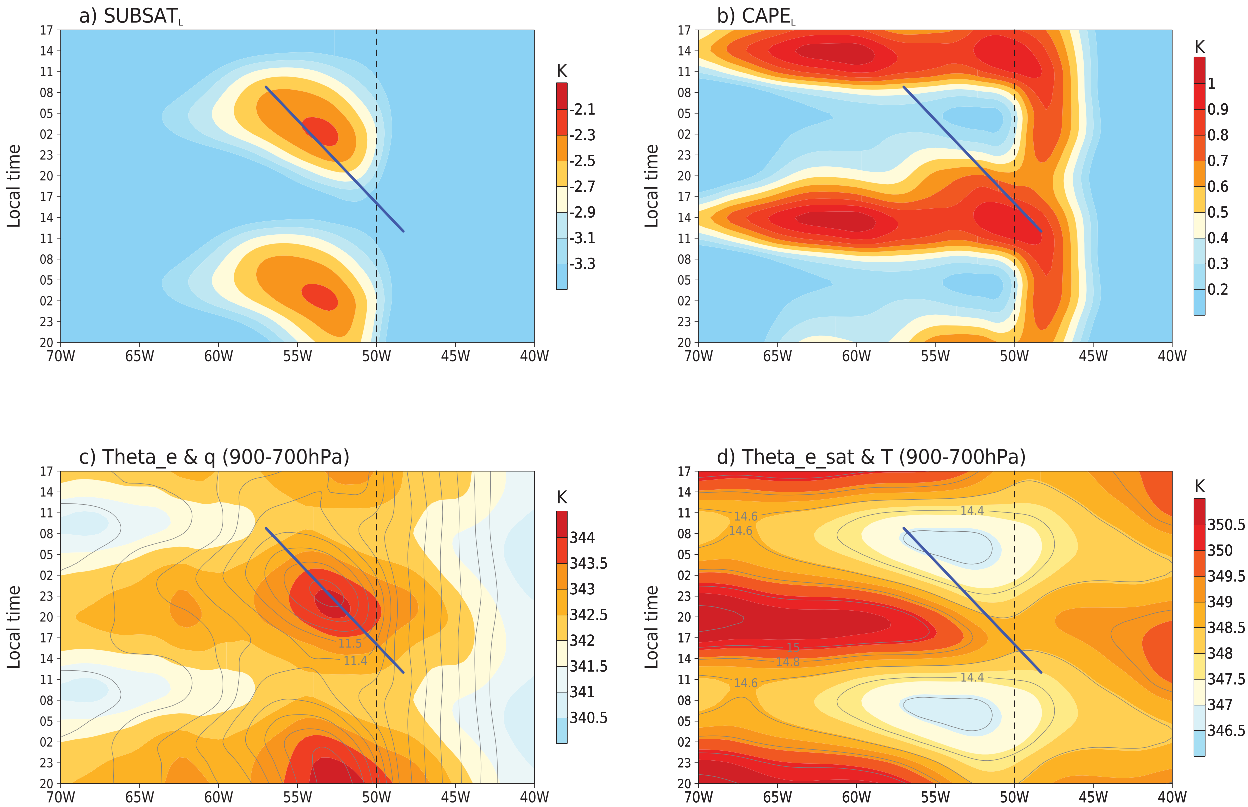

FIG. 7. Diurnal Hovmöller diagrams of (a) SUBSAT$_L$ and (b) CAPE$_L$, the two components of lower-tropospheric buoyancy associated with diurnal evolution of precipitation based on the observed strong diurnal propagation events identified by IMERG. Similar diurnal Hovmöller diagrams of 900–700-hPa averaged θ_e (shading; K) and specific humidity q (contours; g kg^{-1}) are shown in (c), and θ^*_{eL} (shading; K) and temperature (contours; °C) are shown in (d). All variables are plotted along the transect following the blue line in Fig. 3. The blue lines in each panel are copied from Fig. 6a, representing the propagation of precipitation associated with the strong diurnal events. All these variables are based on the ERA5 reanalysis.

Following Ahmed and Neelin (2021), the lower-tropospheric buoyancy B_L is defined as follows:

$$B_L = \frac{g}{\overline{k}_L \theta_{e0}}\left[\underbrace{w_B\left(\frac{\theta_{eB} - \theta^*_{eL}}{\theta^*_{eL}}\right)\theta_{e0}}_{\text{CAPE}_L} - \underbrace{w_L\left(\frac{\theta^*_{eL} - \theta_{eL}}{\theta^*_{eL}}\right)\theta_{e0}}_{\text{SUBSAT}_L}\right] \quad (1)$$

where θ_e is the equivalent potential temperature, and θ_{eB} is θ_e averaged over the boundary layer, defined as the 100-hPa layer above the surface; θ_{eL} and θ^*_{eL} are the θ_e and saturated θ_e averaged over the lower troposphere between the top of the boundary layer and 500 hPa; θ_{e0} is a reference θ_e value of 340 K; $\overline{k}_L$ is a constant of 3.0; and g is the constant of the acceleration due to gravity (9.8 m s^{-2}). The first term of B_L, CAPE$_L$, is a measure of the undiluted plume buoyancy equivalent to the convective available potential energy (CAPE) computed using gridscale vertical stratification between the lower troposphere and the boundary layer. The second term, SUBSAT$_L$, measures the degree of subsaturation in the lower troposphere. Weights w_B and w_L represent relative fractions of mass inflow to the plume in the boundary layer and lower troposphere and are defined as follows:

$$w_B = \frac{\Delta p_B}{\Delta p_L}\ln\left(1 + \frac{\Delta p_L}{\Delta p_B}\right), \quad (2)$$

$$w_L = 1 - w_B, \quad (3)$$

where Δp_L and Δp_B (=100 hPa) are the vertical depth of the lower troposphere and boundary layer, respectively. See Ahmed et al. (2020) and Ahmed and Neelin (2021) for details on the derivation of the above B_L equation.

Figures 7a and 7b illustrate the Hovmöller diagrams of CAPE$_L$ and SUBSAT$_L$ along the transect AB associated with the southwestward propagation of diurnal convection based on composite over strong propagating diurnal events as shown in Fig. 6a. The blue line in each panel of Fig. 7 denotes the propagation of precipitation associated with strong diurnal events, as duplicated following the precipitation Hovmöller diagram in Fig. 6a. It is evident that the triggering of diurnal convection near the coast of northeastern Brazil at noon tends to be associated with the accumulation of CAPE$_L$ due to diurnal surface warming (Fig. 7b). As a systematic westward propagation in CAPE$_L$ is not clearly evident in Fig. 7b, the initial inland progression of the diurnal rain belt near the coastal region during the early afternoon is likely driven by the sea breeze and its induced dynamical convergence (Sousa et al. 2021). The continuous southwestward propagation of diurnal convection during nighttime and the next morning is largely associated with the migration of $SUBSAT_L$ (Fig. 7a). The region of active convection corresponds to small negative values of $SUBSAT_L$, indicating an environment closer to a saturated condition. Since $SUBSAT_L$ is connected to both θ_{eL} and θ^*_{eL} [Eq. (1)], the diurnal evolution of θ_{eL} and θ^*_{eL} along the transect AB is further illustrated in Figs. 7c and 7d (shaded). It can be observed that the westward propagation of reduced negative values of $SUBSAT_L$ over east Amazon is mainly due to enhanced θ_{eL} (Fig. 7c shaded), which in turn closely follows an increase in lower-tropospheric moisture (Fig. 7c contour). Conversely, while θ^*_{eL} is largely influenced by lower-tropospheric temperature variations due to the Clausius–Clapeyron relationship (Fig. 7d contours), it does not exhibit a similar westward propagation as $SUBSAT_L$ (Fig. 7d shaded). However, the reduced θ^*_{eL} over the inland region during nocturnal hours, induced by radiative cooling, helps to maintain a buoyant environment and further promotes the westward propagation of $SUBSAT_L$ and convection after 2300 LT. This may explain why the maximum values of θ_{eL} and q are observed near 2300 LT to the west of 50°W (Fig. 7c), while the maxima of $SUBSAT_L$ and precipitation occur further west between 0200 and 0500 LT (Fig. 7a).

These results suggest that the buoyancy forcing associated with the westward propagation of lower-tropospheric moisture plays a crucial role in driving the systematic westward movement of diurnal convection over east Amazon, particularly during the late afternoon and nighttime, as clearly indicated by Fig. 7c. This result raises an additional question: What factors influence the westward propagation of the lower-tropospheric moisture in this region? To address this question, we analyze the moisture budget terms related to the westward propagation of strong diurnal events using the EC-YOPP dataset. Note that the EC-YOPP dataset only covers two MAM seasons from 2018 to 2019. However, the characteristics of diurnal precipitation and lower-tropospheric moisture (q_L) based on 21 strong propagation events during these two MAM seasons are largely similar to those observed in Figs. 6a and 7c, which are based on all strong events from 2000 to 2019 (figure not shown). Therefore, analyzing the moisture budget based on strong westward-propagating events during 2018–19 will provide valuable insights into the underlying processes that contribute to the westward propagation of moisture and thus diurnal convection over east Amazon.

Figure 8a illustrates a vertical pressure–longitude cross section of moisture tendency along the transect AB at 2300 LT based on the composite over 21 strong westward-propagating diurnal events during MAM of 2018–19. The selection of 2300 LT is primarily based on the consideration that the diurnal moisture signals exhibit the strongest amplitude and propagation at this time (see Fig. 7c contours). Moistening (drying) occurs in the lower-troposphere between 900 and 500 hPa to the west (east) of the convection center (Fig. 8a), consistent with the westward propagation of q_L and convection discussed previously. Figure 8b further illustrates longitudinal profiles of the total moisture budget term averaged between 900 and 500 hPa, along with its contributions from total dynamical and physical processes. The moisture tendency due to physical processes primarily acts as a moisture sink, due to the condensation of water vapor, with its maximum negative value largely collocated with the convection center. Conversely, the maximum moistening due to dynamical processes has a shift to the west of the convection center, i.e., it leads the convection for a westward-propagating system. Further decomposition of the total moisture tendency by dynamical processes into components of horizontal and vertical advection suggests that the westward shift in total moistening (black line) relative to the convection center is mainly driven by the horizontal advection (blue dashed line). Moistening from vertical advection (blue solid line), on the other hand, is largely in phase with convection and balanced by the moisture tendency due to physical processes (Fig. 8b). This moisture budget analysis suggests that the westward propagation of q_L over east Amazon is primarily a result of horizontal moisture advection in the lower troposphere, which is driven by the easterly flow in this region (Fig. 8c), known as the Amazonia low-level jet reported in recent studies (e.g., Anselmo et al. 2020; Bai and Schumacher 2021). As previously discussed, the westward migration of near-saturated air during the nocturnal period toward the inland helps maintain the systematic westward propagation of the diurnal rain belt over east Amazon.

d. Simulations of the diurnal cycle of rainfall over east Amazon in RR-CAM6 simulations

Previous analyses suggest that significant dry biases in climate models over east Amazon can be closely linked to their inability to accurately depict the diurnal cycle of precipitation. Additionally, observations show that the systematic westward propagation of diurnal convection inland in east Amazon is primarily driven by lower-tropospheric buoyancy forcing associated with horizontal moisture advection from the easterly Amazonian low-level jet. With these findings in mind, based on various high-resolution simulations from the RR-CAM6 experiments, this section explores whether increasing the horizontal resolution in models can improve the representation of the diurnal cycle of precipitation and the associated seasonal mean precipitation over east Amazon. Furthermore, we investigate the underlying processes that contribute to this potential improvement. Addressing these questions will provide valuable insights for advancing model development toward improved climate simulations over east Amazon.

Figure 9 illustrates the seasonal mean precipitation patterns across various RR-CAM6 simulations at different horizontal resolutions along with IMERG observations during the three MAM seasons: 2011, 2016, and 2019. Note that the Zhang–McFarlane cumulus scheme remains active for all these RR-CAM6 experiments. In the RR-CAM6 ne30 experiment, the horizontal resolution for the regionally refined grids over South America largely matches that in CAM6+ (~100 km). Note that in the RR-CAM6 experiments, model variables are nudged toward the hourly ERA5 reanalysis during the integration beyond the regionally refined area over South America, unlike the free run in CAM6+.

Similar to CAM6+, the coarse-resolution RR-CAM6 simulations exhibit a dry bias over east Amazon (Figs. 9b,c). However, in the high-resolution RR-CAM6 simulations, this dry bias over east Amazon is significantly reduced (Figs. 9d–f). Meanwhile, the excessive precipitation over the coastal region

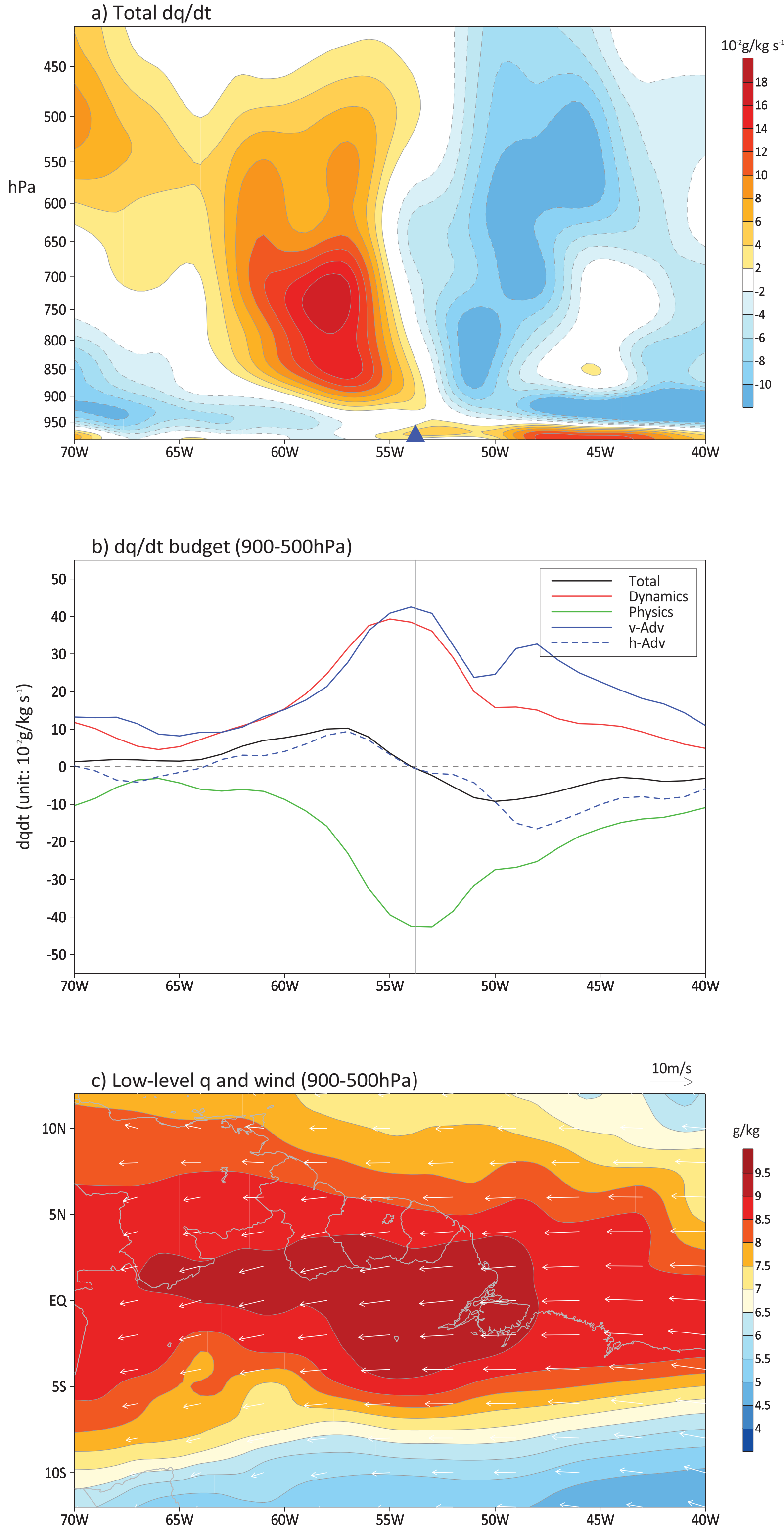

FIG. 8. (a) Longitude–pressure cross section of total moisture tendency at 2300 LT associated with strong diurnal propagation events along the transect AB in Fig. 3. The blue solid triangle denotes the location of the maximum precipitation based on IMERG. (b) Longitudinal profiles of the total moisture tendency (black) averaged over the lower troposphere between 850 and 450 hPa and its decomposition, including moisture

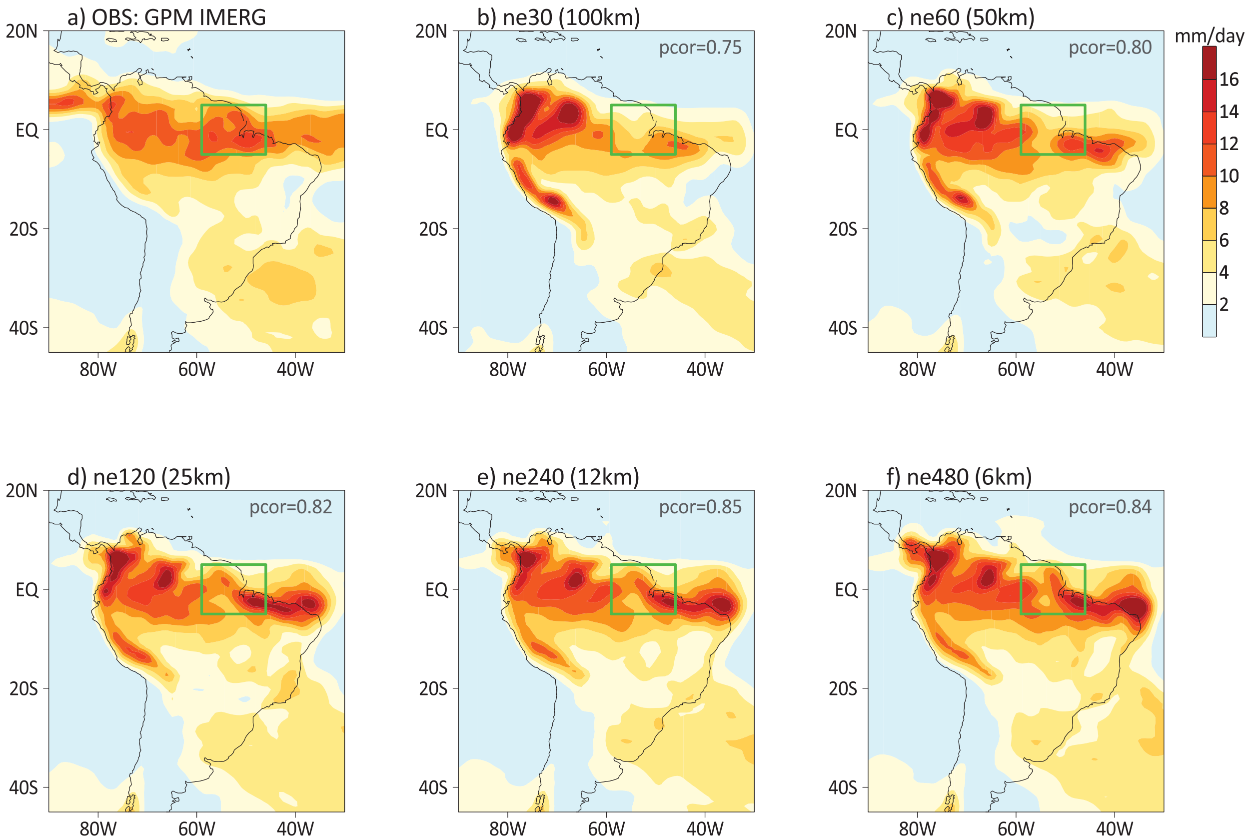

FIG. 9. As in Fig. 1, but for MAM seasonal mean precipitation based on IMERG and various RR-CAM6 experiments during the 3 years of 2011, 2016, and 2019. Pattern correlation coefficients between simulated and observed mean precipitation patterns are shown on the upper right of each panel.

of Ecuador and near the Andes is also somewhat alleviated with the increased horizontal resolution in the model. Notably, the pattern correlation score for MAM mean precipitation across South America increases gradually with increasing model resolution in these RR-CAM6 experiments (Fig. 9). Additionally, note that the anomalously strong precipitation offshore of the easternmost tip of Brazil in RR-CAM6 simulations is likely a numerical artifact resulting from the grid transition between the high-resolution South American domain and the coarser 1° grid outside this region.

To confirm whether the improved seasonal mean precipitation pattern over east Amazon in high-resolution RR-CAM6 simulations is associated with improved representation of the diurnal cycle of precipitation, Fig. 10 shows the 3-hourly evolution of precipitation patterns over east Amazon, based on the climatological diurnal cycle derived from various RR-CAM6 simulations along with IMERG observations during three MAM seasons. The main characteristics of the observed diurnal cycle of precipitation over east Amazon during these 3 years (Fig. 10a) are broadly consistent with those observed over the entire period of 2010–19 (Fig. 3a), suggesting that the climatological diurnal cycle from the 3 years of RR-CAM6 simulations is robust. As shown in Fig. 10b, the well-organized rain belt observed along the coastal region of east Amazon is poorly simulated in the ne30 experiment, resulting in a significant dry bias over the green box region of east Amazon. Additionally, the previously discussed southwestward-propagating diurnal convection signals are largely absent in ne30 simulations, as clearly illustrated by the diurnal Hovmöller diagrams (cf. Figs. 11a,b). This finding supports the earlier discussions based on CAM6+ about the crucial role of diurnal convective activity in influencing seasonal mean precipitation over east Amazon.

In the RR-CAM6 experiments, increasing the horizontal resolution over South America leads to improved representation of the rain belt over the coastal region of east Amazon, especially in the three experiments with a horizontal resolution

←
tendency due to dynamical processes (red), physical processes (green), horizontal (blue dashed), and vertical (blue solid) advection. (c) Spatial distribution of 900–500-hPa averaged moisture (shaded) and winds (vectors) at 2300 LT. All these fields are based on the EC-YOPP analysis dataset.

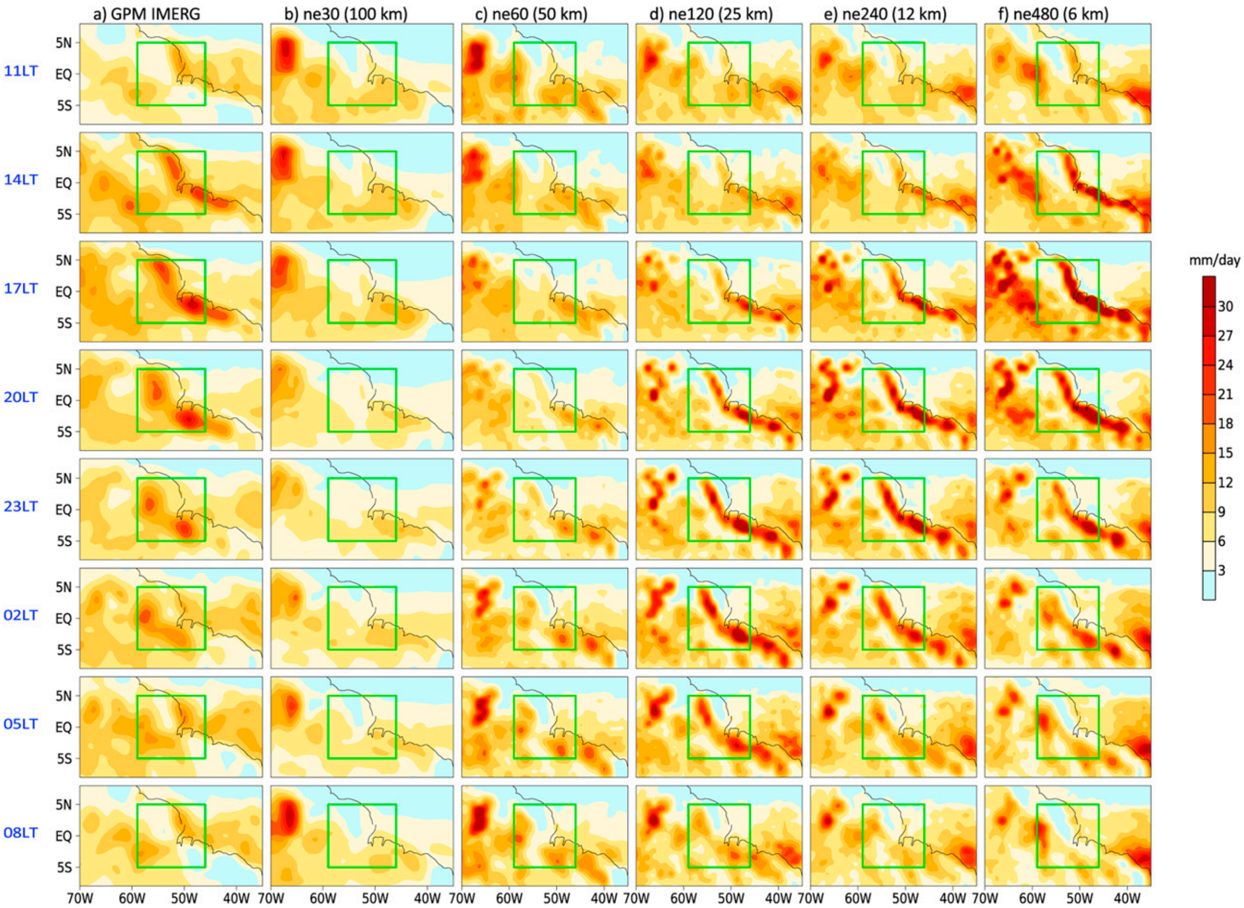

FIG. 10. As in Fig. 3, but for the diurnal evolution of precipitation based on (a) IMERG and the RR-CAM6 simulations at various horizontal resolutions: (b) ne30, (c) ne60, (d) ne120, (e) ne240, and (f) ne480. The climatological diurnal cycle of precipitation for both observations and RR-CAM6 experiments is derived based on MAM during the 3 years of 2011, 2016, and 2019.

higher than 25 km: ne120, ne240, and ne480 (Figs. 10d–f). The experiment ne480, in particular, successfully captures the formation of a strong rain belt over the coastal region after 1400 LT, followed by its intensification and southwestward propagation inland (Fig. 10f). However, there are also some limitations in the simulated precipitation diurnal cycle in these high-resolution RR-CAM6 experiments. For instance, the rain belt in the ne240 and ne480 simulations tends to be narrower compared to observations (cf. the rain belt in the green box region at 1700 LT in Fig. 10, between the model and observations). This result suggests potential deficiencies in the model's ability to accurately depict the organization of convection associated with the diurnal rain belt, possibly related to the detailed structures of the land-sea breezes. Additionally, although the representation of the southwestward propagation of the rain belt over east Amazon improves with higher horizontal resolution in the RR-CAM6 simulations, it remains weaker and less coherent in the ne480 experiment during local afternoon and early evening compared to observations (cf. Figs. 11a,f).

We then ask why the diurnal evolution of precipitation over east Amazon, particularly the westward propagation of diurnal convection, is better represented in the higher-resolution RR-CAM6 simulations. Since previous observational analyses suggest that the buoyancy forcing associated with the lower-tropospheric moisture plays a crucial role in this westward propagation, Fig. 11 displays Hovmöller diagrams of q_L from various RR-CAM6 simulations along with that based on the ERA5 reanalysis. The gradual westward migration of q_L toward the inland during the nocturnal time is again clearly evident in ERA5 (Fig. 12a), as previously discussed in Figs. 7c and 8. While the westward propagation of q_L is discerned in all the RR-CAM6 simulations (Figs. 12b–f), it is less coherent than ERA5. Particularly, in contrast to the diurnal q_L maximum over the inland region to the west of 50°W near 2300 LT in ERA5 (Fig. 12a), it occurs in the local afternoon slightly west of the coastline in all RR-CAM6 simulations. The lack of systematic westward migration of q_L in RR-CAM6 simulations could be responsible for the aforementioned less coherent westward propagation of rain belt during the nocturnal time in the high-resolution RR-CAM6 (Fig. 11f). Interestingly, despite the fact that the westward propagation of convection is only captured in the higher resolution of RR-CAM6 simulations, the propagation features in q_L are not sensitive to model's

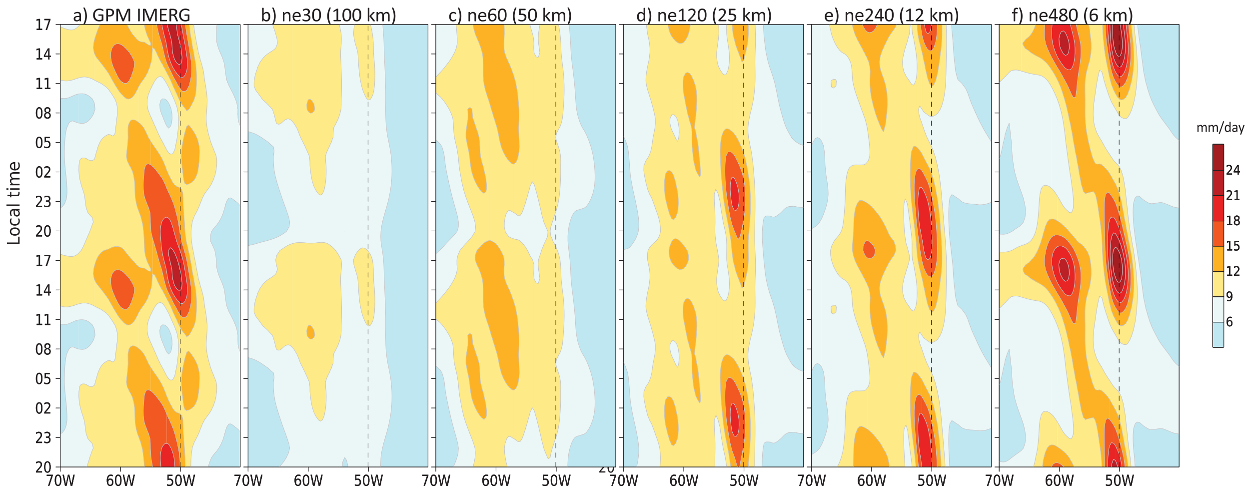

FIG. 11. The Hovmöller diagrams of diurnal precipitation along the transect AB based on IMERG and various RR-CAM6 experiments. The diurnal cycle of precipitation shown here is based on the MAM seasons of 2011, 2016, and 2019.

horizontal resolution and are largely similar across these RR-CAM6 experiments (Fig. 11). Meanwhile, a reduced amplitude in q_L is found in the higher-resolution RR-CAM6 simulations, which will be further discussed. The fact that the westward propagation of diurnal q_L is simulated in the lower-resolution RR-CAM6 simulations, while diurnal convection signals are not, implies that convective activity in response to lower-tropospheric diurnal buoyancy fluctuations could only be accurately captured in high-resolution simulations.

Motivated by the results shown in Fig. 12, we further illustrate the relationship between the lower-tropospheric buoyancy B_L and total precipitation over east Amazon in various RR-CAM6 simulations (Fig. 13). Consistent with our earlier hypothesis, the sensitivity of precipitation in response to B_L is strongly dependent on the model's horizontal resolution. In high-resolution RR-CAM6 simulations, total precipitation is highly sensitive to changes in B_L, whereas this sensitivity is dramatically reduced in the lower-resolution RR-CAM6 simulations. A closer examination of the relationship between B_L and both convective precipitation and large-scale precipitation suggests that the high sensitivity of total precipitation in high-resolution RR-CAM6 simulations primarily stems from changes in large-scale precipitation (Fig. 13d, also see Fig. S3). In contrast, while convective precipitation is generally much weaker than large-scale precipitation, its response to B_L slightly weakens with an increase in model resolution (Fig. 13c).

The greater sensitivity of large-scale precipitation to lower-tropospheric buoyancy forcing in high-resolution RR-CAM6 simulations aligns with the findings from previous studies (e.g., Jeevanjee 2017; O'Brien et al. 2016; Rauscher et al. 2016; Donner et al. 2016; Herrington and Reed 2018, 2020). It has been suggested that the increase in large-scale precipitation in high-resolution simulations is closely related to an increase in upward moisture flux at cloud base, which corresponds to stronger

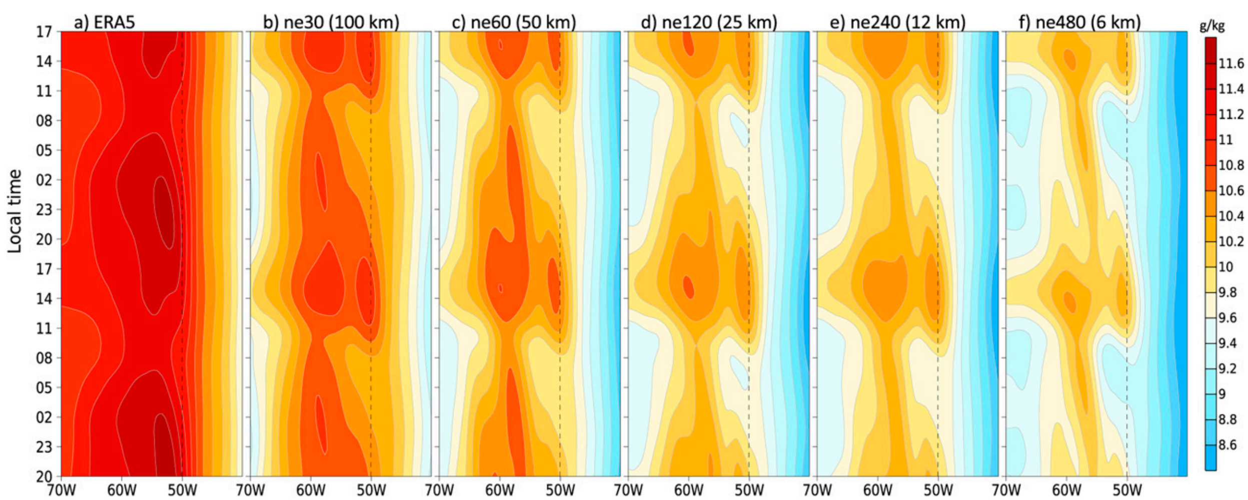

FIG. 12. As in Fig. 11, but for the Hovmöller diagrams of lower-tropospheric specific humidity averaged between 900 and 700 hPa along the transect AB based on ERA5 and various RR-CAM6 experiments.

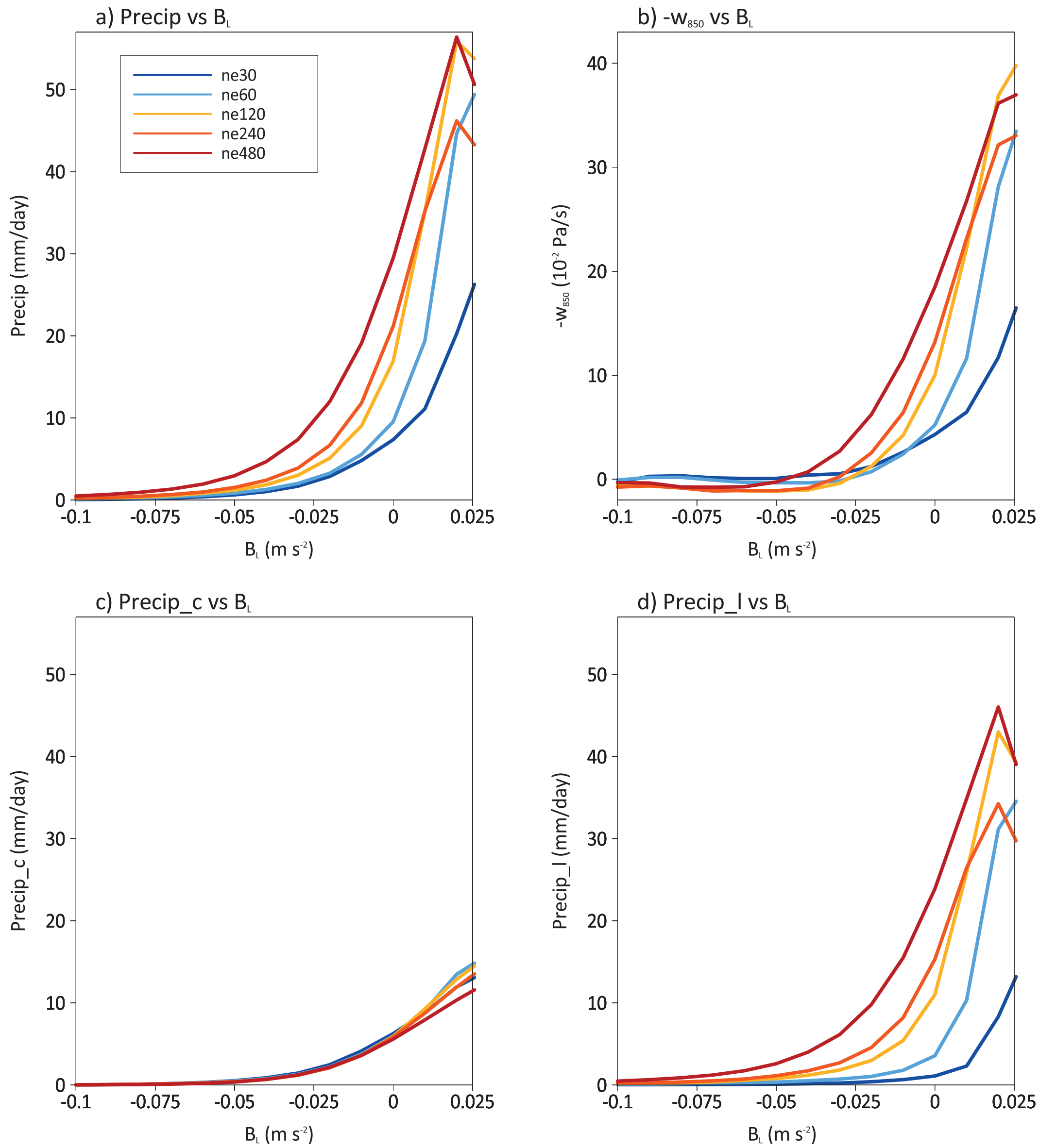

FIG. 13. Composite of (a) total precipitation, (b) 850-hPa vertical velocity (omega) with sign reversed, (c) convective precipitation, and (d) large-scale precipitation as a function of the lower-tropospheric buoyancy over east Amazon in various RR-CAM6 experiments based on hourly model output during MAM of the 3 years (2011, 2016, and 2019).

vertical velocities in high-resolution models (Fig. 13b), following an analytic scaling derived for the equations of motion at hydrostatic scales (Herrington and Reed 2018, 2020). Additionally, the stronger compensating subsidence associated with enhanced large-scale heating in high-resolution simulations enhances atmospheric stability and downward advection of dry air aloft, thereby reducing parameterized convective precipitation (Herrington and Reed 2020), a finding also supported by simulations in RR-CAM6. Meanwhile, a drier atmosphere, due to the stronger compensating subsidence in the higher-resolution simulations as suggested in previous studies (e.g., Herrington and Reed 2020), is also consistent with the RR-CAM6 simulations in Fig. 12.

4. Summary and discussion

Precipitation in the Amazon basin is vital for global hydrological and carbon cycles. However, current global climate models exhibit significant flaws in simulating the mean precipitation pattern in this region, particularly a consistent dry bias over east Amazon during the local rainy season from March to May (MAM). This study, based on simulations from a developmental version of the CAM6 model (CAM6+), reveals that the dry bias in MAM mean precipitation for east Amazon can be linked to the model's deficiencies in depicting the diurnal evolution of rainfall near the northeastern Brazil coast. These include the formation of a rain belt along the coastal area around noon and its subsequent southwestward movement inland during the afternoon and nighttime. By using a recently proposed precipitation-buoyancy framework, we demonstrate that the observed systematic southwestward movement of diurnal convection over east Amazon is closely tied to horizontal moisture advection from the easterly Amazonian low-level jet, which creates a buoyant environment with a lower moisture deficit on the western side of the convection center. The westward-propagating diurnal rain belt can be further amplified as it travels over the inland region during nighttime due to lower-tropospheric cooling and thus reduced θ^*_{eL}.

Model deficiencies in depicting the diurnal cycle of precipitation and mean precipitation over east Amazon can be attributed to both limitations in physical parameterization schemes and the coarse horizontal resolution of these models. To investigate whether higher model resolution can improve simulations of regional precipitation variability over east Amazon, we analyzed results from regionally refined CAM6 (RR-CAM6) experiments. The findings indicate that the diurnal evolution of precipitation over east Amazon, including the formation of an elongated rain belt along the coast around noon and its southwestward migration inland, is particularly evident in the ne480 experiment, which has an equivalent resolution of ~6 km over South America. Along with the improved diurnal cycle of precipitation, the high-resolution RR-CAM6 simulations also produce more accurate MAM seasonal mean precipitation patterns, reducing dry biases over east Amazon and confirming the important role of the diurnal cycle for seasonal mean precipitation in this region.

Further analyses suggest that the improved simulations of diurnal rainfall over east Amazon in high-resolution RR-CAM6 simulations are due to a significantly increased sensitivity of large-scale precipitation to fluctuations in lower-tropospheric buoyancy, contrasting with a slight reduction in convective precipitation in the higher-resolution RR-CAM6 simulations. While a higher resolution model is expected to better resolve local circulation patterns, such as land–sea breezes near the coast, the easterly Amazonian low-level jet and its induced westward propagation of lower-tropospheric moisture and buoyancy are largely simulated in all RR-CAM6 experiments, even at coarser resolutions (Fig. S4). However, a weak sensitivity of convection to lower-tropospheric buoyancy forcing results in a considerable absence of systematic westward propagation of precipitation in coarse-resolution models.

Although this study offers important insights for improving climate simulations over east Amazon by emphasizing the necessity of high-resolution modeling, the metrics identified in this study on the sensitivity of precipitation to the lower-tropospheric buoyancy can also be useful in testing and developing deep convection parameterizations in coarse-resolution models (such as CAM6+) to reduce precipitation bias over the Amazon region. For example, more realistic simulations of the propagating convection system over the central United States in coarse-resolution models using the Grell scheme (Grell 1993; Grell and Freitas 2014) could be ascribed to the responsiveness of the Grell scheme to large-scale tropospheric forcing (Liang et al. 2004; Jiang et al. 2006; Gao et al. 2017). Additionally, the improved representation of diurnal propagating signals in the Department of Energy's Energy Exascale Earth System Model (E3SM) may be attributed to the enhanced depiction of the precipitation-buoyancy relationship through the modified convection triggers in the Zhang–McFarlane scheme (Xie et al. 2019).

Despite its overall improvement over coarser-resolution simulations, notable deficiencies in depicting the diurnal cycle of precipitation over east Amazon remain evident in the 6-km RR-CAM6 simulations. For instance, the organization of the diurnal rain belt over coastal land in the afternoon is too narrow compared to observations, and its southwestward propagation inland is relatively weak and confined to the coastal region, unlike the more extensive propagation observed during the late afternoon and early evening. Meanwhile, all the RR-CAM6 simulations show deficiencies in depicting the observed gradual westward migration of diurnal lower-tropospheric moisture, which may also contribute to the less coherent westward propagation of the diurnal rain belt captured in the high-resolution RR-CAM6 simulations. Besides horizontal resolution, these model deficiencies may also be linked to model physics, including processes such as convection triggering, vertical mixing over the land surface, and cloud-radiation feedbacks. Future investigations are needed to understand how improvements in model physics can further enhance the representation of the diurnal cycle and the mean state of precipitation over east Amazon in high-resolution models. While this study primarily focuses on the diurnal cycle of precipitation, examining the detailed characteristics of mesoscale convective systems (e.g., Bai and Schumacher 2021; Feng et al. 2021) in global cloud-resolving models at resolutions finer than 6 km, such as those participating in the Dynamics of the Atmospheric General Circulation Modeled On Nonhydrostatic Domains (DYAMOND) project (Stevens et al. 2019), can provide further insights into improving the modeling of regional precipitation patterns over east Amazon.

Acknowledgments. Part of this work was conducted at the Jet Propulsion Laboratory, California Institute of Technology, under a contract with NASA (80NM0018D0004). This study was supported by the NSF Climate Process Team Program through Grant AGS-1916619. X. J. also acknowledges partial support by the Regional and Global Model Analysis Program of U.S. Department of Energy under Award DE-SC0024315. We thank Dr. Courtney Schumacher and two anonymous reviewers for insightful comments on an earlier version of this manuscript.

Data availability statement. The GPM IMERG rainfall data can be accessed from the website: https://disc.gsfc.nasa.gov/datasets/GPM_3IMERGHH_07/summary. The ERA5 data can be downloaded from the website https://cds.climate.copernicus.eu/datasets/reanalysis-era5-pressure-levels. The EC-YOPP dataset was downloaded from https://www.ecmwf.int/en/forecasts/dataset/year-polar-prediction, but the public service for this dataset has been decommissioned on 1 June 2023. The primary processed data detailing climatological diurnal cycle, derived from both observations and CAM6+ simulations, are available at https://ucla.box.com/v/amazon-diurnal-cycle. Due to project data sharing policies and the exceptionally large data volume, the high-resolution RR-CAM6 outputs are not publicly available at this time but can be made available upon reasonable request to the corresponding authors.

REFERENCES

Adames, Á. F., S. W. Powell, F. Ahmed, V. C. Mayta, and J. D. Neelin, 2021: Tropical precipitation evolution in a buoyancy-budget framework. *J. Atmos. Sci.*, **78**, 509–528, https://doi.org/10.1175/JAS-D-20-0074.1.

Ahmed, F., and J. D. Neelin, 2018: Reverse engineering the tropical precipitation–buoyancy relationship. *J. Atmos. Sci.*, **75**, 1587–1608, https://doi.org/10.1175/JAS-D-17-0333.1.

——, and ——, 2021: A process-oriented diagnostic to assess precipitation-thermodynamic relations and application to CMIP6 models. *Geophys. Res. Lett.*, **48**, e2021GL094108, https://doi.org/10.1029/2021GL094108.

——, N F. Adames, and J. D. Neelin, 2020: Deep convective adjustment of temperature and moisture. *J. Atmos. Sci.*, **77**, 2163–2186, https://doi.org/10.1175/JAS-D-19-0227.1.

Anselmo, E. M., C. Schumacher, and L. A. T. Machado, 2020: The Amazonian low-level jet and its connection to convective cloud propagation and evolution. *Mon. Wea. Rev.*, **148**, 4083–4099, https://doi.org/10.1175/MWR-D-19-0414.1.

——, L. A. T. Machado, C. Schumacher, and G. N. Kiladis, 2021: Amazonian mesoscale convective systems: Life cycle and propagation characteristics. *Int. J. Climatol.*, **41**, 3968–3981, https://doi.org/10.1002/joc.7053.

Bai, H., and C. Schumacher, 2021: The interaction between the nocturnal Amazonian low-level jet and convection in CESM. *J. Climate*, **34**, 8519–8532, https://doi.org/10.1175/JCLI-D-21-0042.1.

Bambach, N. E., A. M. Rhoades, B. J. Hatchett, A. D. Jones, P. A. Ullrich, and C. M. Zarzycki, 2022: Projecting climate change in South America using variable-resolution community Earth system model: An application to Chile. *Int. J. Climatol.*, **42**, 2514–2542, https://doi.org/10.1002/joc.7379.

Bauer, P., I. Sandu, L. Magnusson, R. Mladek, and M. Fuentes, 2020: ECMWF global coupled atmosphere, ocean and sea-ice dataset for the Year of Polar Prediction 2017–2020. *Sci. Data*, **7**, 427, https://doi.org/10.1038/s41597-020-00765-y.

Biasutti, M., D. S. Battisti, and E. S. Sarachik, 2005: Terrestrial influence on the annual cycle of the Atlantic ITCZ in an AGCM coupled to a slab ocean model. *J. Climate*, **18**, 211–228, https://doi.org/10.1175/JCLI3262.1.

Burleyson, C. D., Z. Feng, S. M. Hagos, J. Fast, L. A. T. Machado, and S. T. Martin, 2016: Spatial variability of the background diurnal cycle of deep convection around the GoAmazon2014/5 field campaign sites. *J. Appl. Meteor. Climatol.*, **55**, 1579–1598, https://doi.org/10.1175/JAMC-D-15-0229.1.

Caldwell, A. P. M., and Coauthors, 2021: Convection-permitting simulations with the E3SM global atmosphere model. *J. Adv. Model. Earth Syst.*, **13**, e2021MS002544, https://doi.org/10.1029/2021MS002544.

Cohen, J. C. P., M. A. F. Silva Dias, and C. A. Nobre, 1995: Environmental conditions associated with Amazonian squall lines: A case study. *Mon. Wea. Rev.*, **123**, 3163–3174, https://doi.org/10.1175/1520-0493(1995)123<3163:ECAWAS>2.0.CO;2.

Cox, P. M., R. A. Betts, M. Collins, P. P. Harris, C. Huntingford, and C. D. Jones, 2004: Amazonian forest dieback under climate-carbon cycle projections for the 21st century. *Theor. Appl. Climatol.*, **78**, 137–156, https://doi.org/10.1007/s00704-004-0049-4.

Cui, Z., G. J. Zhang, Y. Wang, and S. Xie, 2021: Understanding the roles of convective trigger functions in the diurnal cycle of precipitation in the NCAR CAM5. *J. Climate*, **34**, 6473–6489, https://doi.org/10.1175/JCLI-D-20-0699.1.

Danabasoglu, G., and Coauthors, 2020: The Community Earth System Model Version 2 (CESM2). *J. Adv. Model. Earth Syst.*, **12**, e2019MS001916, https://doi.org/10.1029/2019MS001916.

Donner, L. J., T. A. O'Brien, D. Rieger, B. Vogel, and W. F. Cooke, 2016: Are atmospheric updrafts a key to unlocking climate forcing and sensitivity? *Atmos. Chem. Phys.*, **16**, 12 983–12 992, https://doi.org/10.5194/acp-16-12983-2016.

Feng, Z., and Coauthors, 2021: A global high-resolution mesoscale convective system database using satellite-derived cloud tops, surface precipitation, and tracking. *J. Geophys. Res. Atmos.*, **126**, e2020JD034202, https://doi.org/10.1029/2020JD034202.

Field, C. B., M. J. Behrenfeld, J. T. Randerson, and P. Falkowski, 1998: Primary production of the biosphere: Integrating terrestrial and oceanic components. *Science*, **281**, 237–240, https://doi.org/10.1126/science.281.5374.237.

Foley, J. A., A. Botta, M. T. Coe, and M. H. Costa, 2002: El Niño–Southern Oscillation and the climate, ecosystems and rivers of Amazonia. *Global Biogeochem. Cycles*, **16**, 1132, https://doi.org/10.1029/2002GB001872.

Friedlingstein, P., and Coauthors, 2006: Climate–carbon cycle feedback analysis: Results from the C4MIP model intercomparison. *J. Climate*, **19**, 3337–3353, https://doi.org/10.1175/JCLI3800.1.

——, and Coauthors, 2014: Persistent growth of CO_2 emissions and implications for reaching climate targets. *Nat. Geosci.*, **7**, 709–715, https://doi.org/10.1038/ngeo2248.

Fu, R., and Coauthors, 2013: Increased dry-season length over southern Amazonia in recent decades and its implication for future climate projection. *Proc. Natl. Acad. Sci. USA*, **110**, 18 110–18 115, https://doi.org/10.1073/pnas.1302584110.

Gao, Y., L. R. Leung, C. Zhao, and S. Hagos, 2017: Sensitivity of U.S. summer precipitation to model resolution and convective parameterizations across gray zone resolutions. *J. Geophys. Res. Atmos.*, **122**, 2714–2733, https://doi.org/10.1002/2016JD025896.

Garreaud, R., and J. M. Wallace, 1997: The diurnal march of convective cloudiness over the Americas. *Mon. Wea. Rev.*, **125**, 3157–3171, https://doi.org/10.1175/1520-0493(1997)125<3157:TDMOCC>2.0.CO;2.

Gent, P. R., and Coauthors, 2011: The Community Climate System Model version 4. *J. Climate*, **24**, 4973–4991, https://doi.org/10.1175/2011JCLI4083.1.

Gettelman, A., and H. Morrison, 2015: Advanced two-moment bulk microphysics for global models. Part I: Off-line tests and comparison with other schemes. *J. Climate*, **28**, 1268–1287, https://doi.org/10.1175/JCLI-D-14-00102.1.

Golaz, J.-C., V. E. Larson, and W. R. Cotton, 2002: A PDF-based model for boundary layer clouds. Part I: Method and model description. *J. Atmos. Sci.*, **59**, 3540–3551, https://doi.org/10.1175/1520-0469(2002)059<3540:APBMFB>2.0.CO;2.

Grell, G. A., 1993: Prognostic evaluation of assumptions used by cumulus parameterizations. *Mon. Wea. Rev.*, **121**, 764–787, https://doi.org/10.1175/1520-0493(1993)121<0764:PEOAUB>2.0.CO;2.

Grell, G. A., and S. R. Freitas, 2014: A scale and aerosol aware stochastic convective parameterization for weather and air quality modeling. *Atmos. Chem. Phys.*, **14**, 5233–5250, https://doi.org/10.5194/acp-14-5233-2014.

Hagos, S. M., L. R. Leung, O. A. Garuba, C. Demott, B. Harrop, J. Lu, and M.-S. Ahn, 2021: The relationship between precipitation and precipitable water in CMIP6 simulations and implications for tropical climatology and change. *J. Climate*, **34**, 1587–1600, https://doi.org/10.1175/JCLI-D-20-0211.1.

Herrington, A. R., and K. A. Reed, 2018: An idealized test of the response of the Community Atmosphere Model to near-grid-scale forcing across hydrostatic resolutions. *J. Adv. Model. Earth Syst.*, **10**, 560–575, https://doi.org/10.1002/2017MS001078.

——, and ——, 2020: On resolution sensitivity in the Community Atmosphere Model. *Quart. J. Roy. Meteor. Soc.*, **146**, 3789–3807, https://doi.org/10.1002/qj.3873.

Hersbach, H., and Coauthors, 2020: The ERA5 global reanalysis. *Quart. J. Roy. Meteor. Soc.*, **146**, 1999–2049, https://doi.org/10.1002/qj.3803.

Huffman, G., D. T. Bolvin, E. J. Nelkin, and J. Tan, 2019: Integrated Multi-satellitE Retrievals for GPM (IMERG) technical documentation. NASA Tech. Doc., 77 pp., https://gpm.nasa.gov/sites/default/files/document_files/IMERG_doc_190909.pdf.

Hurrell, J. W., J. J. Hack, D. Shea, J. M. Caron, and J. Rosinski, 2008: A new sea surface temperature and sea ice boundary dataset for the Community Atmosphere Model. *J. Climate*, **21**, 5145–5153, https://doi.org/10.1175/2008JCLI2292.1.

Iacono, M. J., J. S. Delamere, E. J. Mlawer, M. W. Shephard, S. A. Clough, and W. D. Collins, 2008: Radiative forcing by long-lived greenhouse gases: Calculations with the AER radiative transfer models. *J. Geophys. Res.*, **113**, D13103, https://doi.org/10.1029/2008JD009944.

Jeevanjee, N., 2017: Vertical velocity in the gray zone. *J. Adv. Model. Earth Syst.*, **9**, 2304–2316, https://doi.org/10.1002/2017MS001059.

Jiang, X., and B. Tian, 2024: Tropical meteorology: Intertropical convergence zone. *Reference Module in Earth Systems and Environmental Sciences*, Elsevier, 355–367.

——, N.-C. Lau, and S. A. Klein, 2006: Role of eastward propagating convection systems in the diurnal cycle and seasonal mean of summertime rainfall over the U.S. Great Plains. *Geophys. Res. Lett.*, **33**, L19809, https://doi.org/10.1029/2006GL027022.

Kousky, V. E., 1980: Diurnal rainfall variation in northeast Brazil. *Mon. Wea. Rev.*, **108**, 488–498, https://doi.org/10.1175/1520-0493(1980)108<0488:DRVINB>2.0.CO;2.

Larson, V. E., 2017: CLUBB-SILHS: A parameterization of subgrid variability in the atmosphere. arXiv 1711.03675v4, https://doi.org/10.48550/arXiv.1711.03675.

Lawrence, D. M., and Coauthors, 2019: The Community Land Model version 5: Description of new features, benchmarking, and impact of forcing uncertainty. *J. Adv. Model. Earth Syst.*, **11**, 4245–4287, https://doi.org/10.1029/2018MS001583.

Li, W., R. Fu, and R. E. Dickinson, 2006: Rainfall and its seasonality over the amazon in the 21st century as assessed by the coupled models for the IPCC AR4. *J. Geophys. Res.*, **111**, D02111, https://doi.org/10.1029/2005JD006355.

Liang, X.-Z., L. Li, A. Dai, and K. E. Kunkel, 2004: Regional climate model simulation of summer precipitation diurnal cycle over the United States. *Geophys. Res. Lett.*, **31**, L24208, https://doi.org/10.1029/2004GL021054.

Lin, P., Y. Ming, and T. Robinson, 2023: On the resolution sensitivity of equatorial precipitation in a GFDL global atmospheric model. *J. Adv. Model. Earth Syst.*, **15**, e2022MS003300, https://doi.org/10.1029/2022MS003300.

Liu, X., P. L. Ma, H. Wang, S. Tilmes, B. Singh, R. C. Easter, S. J. Ghan, and P. J. Rasch, 2016: Description and evaluation of a new four-mode version of the Modal Aerosol Module (MAM4) within version 5.3 of the Community Atmosphere Model. *Geosci. Model Dev.*, **9**, 505–522, https://doi.org/10.5194/gmd-9-505-2016.

Lober, C., J. Fayne, H. Hashemi, and L. C. Smith, 2023: Bias correction of 20 years of IMERG satellite precipitation data over Canada and Alaska. *J. Hydrol.*, **47**, 101386, https://doi.org/10.1016/j.ejrh.2023.101386.

Meehl, G. A., C. Covey, B. McAvaney, M. Latif, and R. J. Stouffer, 2005: Overview of the coupled model intercomparison project. *Bull. Amer. Meteor. Soc.*, **86**, 89–94, https://doi.org/10.1175/BAMS-86-1-89.

Miura, H., M. Satoh, T. Nasuno, A. T. Noda, and K. Oouchi, 2007: A Madden-Julian Oscillation event realistically simulated by a global cloud-resolving model. *Science*, **318**, 1763–1765, https://doi.org/10.1126/science.1148443.

O'Brien, T. A., W. D. Collins, K. Kashinath, O. Rübel, S. Byna, J. Gu, H. Krishnan, and P. A. Ullrich, 2016: Resolution dependence of precipitation statistical fidelity in hindcast simulations. *J. Adv. Model. Earth Syst.*, **8**, 976–990, https://doi.org/10.1002/2016MS000671.

Oliveira, F. P., and M. D. Oyama, 2020: Squall-line initiation over the northern coast of Brazil in March: Observational features. *Meteor. Appl.*, **27**, e1799, https://doi.org/10.1002/met.1799.

Phillips, O. L., R. J. W. Brienen, and the RAINFOR Collaboration, 2017: Carbon uptake by mature Amazon forests has mitigated Amazon nations' carbon emissions. *Carbon Balance Manage.*, **12**, 1, https://doi.org/10.1186/s13021-016-0069-2.

Rauscher, S. A., T. A. O'Brien, C. Piani, E. Coppola, F. Giorgi, W. D. Collins, and P. M. Lawston, 2016: A multimodel intercomparison of resolution effects on precipitation: Simulations and theory. *Climate Dyn.*, **47**, 2205–2218, https://doi.org/10.1007/s00382-015-2959-5.

Richter, I., and S.-P. Xie, 2008: On the origin of equatorial Atlantic biases in coupled general circulation models. *Climate Dyn.*, **31**, 587–598, https://doi.org/10.1007/s00382-008-0364-z.

——, and H. Tokinaga, 2020: An overview of the performance of CMIP6 models in the tropical Atlantic: Mean state, variability, and remote impacts. *Climate Dyn.*, **55**, 2579–2601, https://doi.org/10.1007/s00382-020-05409-w.

——, S.-P. Xie, S. K. Behera, T. Doi, and Y. Masumoto, 2014: Equatorial Atlantic variability and its relation to mean state biases in CMIP5. *Climate Dyn.*, **42**, 171–188, https://doi.org/10.1007/s00382-012-1624-5.

Sakaguchi, K., and Coauthors, 2023: Technical descriptions of the experimental dynamical downscaling simulations over North America by the CAM–MPAS variable-resolution model. *Geosci. Model Dev.*, **16**, 3029–3081, https://doi.org/10.5194/gmd-16-3029-2023.

Satoh, M., B. Stevens, F. Judt, M. Khairoutdinov, S.-J. Lin, W. M. Putman, and P. Düben, 2019: Global cloud-resolving models. *Curr. Climate Change Rep.*, **5**, 172–184, https://doi.org/10.1007/s40641-019-00131-0.

Silva Dias, M. A. F., and R. N. Ferreira, 1992: Application of a linear spectral model to the study of Amazonian squall lines during GTE/ABLE 2B. *J. Geophys. Res.*, **97**, 20 405–20 419, https://doi.org/10.1029/92JD01333.

Sousa, A. C., L. A. Candido, and P. Satyamurty, 2021: Convective cloud clusters and squall lines along the coastal Amazon. *Mon. Wea. Rev.*, **149**, 3589–3608, https://doi.org/10.1175/MWR-D-21-0045.1.

Stevens, B., and Coauthors, 2019: DYAMOND: The DYnamics of the Atmospheric general circulation Modeled On Non-hydrostatic Domains. *Prog. Earth Planet. Sci.*, **6**, 61, https://doi.org/10.1186/s40645-019-0304-z.

Tai, S.-L., Z. Feng, P.-L. Ma, C. Schumacher, and J. D. Fast, 2021: Representations of precipitation diurnal cycle in the Amazon as simulated by observationally constrained cloud-system resolving and global climate models. *J. Adv. Model. Earth Syst.*, **13**, e2021MS002586, https://doi.org/10.1029/2021MS002586.

Tian, B., and X. Dong, 2020: The double-ITCZ bias in CMIP3, CMIP5, and CMIP6 models based on annual mean precipitation. *Geophys. Res. Lett.*, **47**, e2020GL087232, https://doi.org/10.1029/2020GL087232.

Tozuka, T., T. Doi, T. Miyasaka, N. Keenlyside, and T. Yamagata, 2011: Key factors in simulating the equatorial Atlantic zonal sea surface temperature gradient in a coupled general circulation model. *J. Geophys. Res.*, **116**, C06010, https://doi.org/10.1029/2010JC006717.

Vera, C., G. Silvestri, B. Liebmann, and P. González, 2006: Climate change scenarios for seasonal precipitation in South America from IPCC-AR4 models. *Geophys. Res. Lett.*, **33**, L13707, https://doi.org/10.1029/2006GL025759.

Wang, H., and R. Fu, 2007: The influence of Amazon rainfall on the Atlantic ITCZ through convectively coupled Kelvin waves. *J. Climate*, **20**, 1188–1201, https://doi.org/10.1175/JCLI4061.1.

Xie, S., and Coauthors, 2019: Improved diurnal cycle of precipitation in E3SM with a revised convective triggering function. *J. Adv. Model. Earth Syst.*, **11**, 2290–2310, https://doi.org/10.1029/2019MS001702.

Xie, S.-P., 2023: *Coupled Atmosphere-Ocean Dynamics: From El Niño to Climate Change.* Elsevier, 424 pp.

——, and J. Carton, 2004: Tropical Atlantic variability: Patterns, mechanisms, and impacts. *Earth Climate: The Ocean-Atmosphere Interaction*, *Geophys. Monogr.*, Vol. 147, Amer. Geophys. Union, 121–142.

Yin, L., R. Fu, E. Shevliakova, and R. E. Dickinson, 2013: How well can CMIP5 simulate precipitation and its controlling processes over tropical South America? *Climate Dyn.*, **41**, 3127–3143, https://doi.org/10.1007/s00382-012-1582-y.

Zhang, G. J., and N. A. Mcfarlane, 1995: Sensitivity of climate simulations to the parameterization of cumulus convection in the Canadian Climate Centre general circulation model. *Atmos.–Ocean*, **33**, 407–446, https://doi.org/10.1080/07055900.1995.9649539.

Zhang, K., R. Fu, M. J. Shaikh, S. Ghan, M. Wang, L. R. Leung, R. E. Dickinson, and J. Marengo, 2017: Influence of superparameterization and a higher-order turbulence closure on rainfall bias over Amazonia in Community Atmosphere Model Version 5. *J. Geophys. Res. Atmos.*, **122**, 9879–9902, https://doi.org/10.1002/2017JD026576.

Zhuang, Y., R. Fu, J. A. Marengo, and H. Wang, 2017: Seasonal variation of shallow-to-deep convection transition and its link to the environmental conditions over the central Amazon. *J. Geophys. Res. Atmos.*, **122**, 2649–2666, https://doi.org/10.1002/2016JD025993.